Ice needles weave patterns of stones in freezing landscapes

Anyuan Li[a,b], Norikazu Matsuoka[b], Fujun Niu[c,d], Jing Chen[a], Zhenpeng Ge[e], Wensi Hu[f], Desheng Li[g], Bernard Hallet[h], Johan van de Koppel[i,j], Nigel Goldenfeld[k], and Quan-Xing Liu (刘权兴)[e,f,1]

[a]Key Laboratory of Rock Mechanics and Geohazards of Zhejiang Province, College of Civil Engineering, Shaoxing University, 312000 Shaoxing, China; [b]Faculty of Life and Environmental Sciences, University of Tsukuba, Tsukuba 305-0006, Japan; [c]State Key Laboratory of Frozen Soil Engineering, Northwest Institute of Eco-Environmental and Resources, Chinese Academy of Sciences, 730000 Lanzhou, China; [d]South China Institution of Geotechnical Engineering, School of Civil Engineering and Transportation, South China University of Technology, 510641 Guangzhou, China; [e]School of Ecological and Environmental Sciences, East China Normal University, 200241 Shanghai, China; [f]State Key Laboratory of Estuarine and Coastal Research, East China Normal University, 200241 Shanghai, China; [g]State Key Laboratory of Ocean Engineering, Shanghai Jiao Tong University, 200240 Shanghai, China; [h]Department of Earth and Space Sciences and Quaternary Research Center, University of Washington, Seattle, WA 98195; [i]Royal Netherlands Institute for Sea Research and Utrecht University, 4400 AC, Yerseke, The Netherlands; [j]Groningen Institute for Evolutionary Life Sciences, University of Groningen, 9700 CC Groningen, The Netherlands; and [k]Department of Physics, University of Illinois at Urbana–Champaign, Urbana, IL 61801

Edited by Andrea Rinaldo, Ecole Polytechnique Federale de Lausanne, Lausanne, Switzerland, and approved August 26, 2021 (received for review June 9, 2021)

Patterned ground, defined by the segregation of stones in soil according to size, is one of the most strikingly self-organized characteristics of polar and high-alpine landscapes. The presence of such patterns on Mars has been proposed as evidence for the past presence of surface liquid water. Despite their ubiquity, the dearth of quantitative field data on the patterns and their slow dynamics have hindered fundamental understanding of the pattern formation mechanisms. Here, we use laboratory experiments to show that stone transport is strongly dependent on local stone concentration and the height of ice needles, leading effectively to pattern formation driven by needle ice activity. Through numerical simulations, theory, and experiments, we show that the nonlinear amplification of long wavelength instabilities leads to self-similar dynamics that resemble phase separation patterns in binary alloys, characterized by scaling laws and spatial structure formation. Our results illustrate insights to be gained into patterns in landscapes by viewing the pattern formation through the lens of phase separation. Moreover, they may help interpret spatial structures that arise on diverse planetary landscapes, including ground patterns recently examined using the rover Curiosity on Mars.

sorted patterned ground | phase separation | ice needles | periglacial landform | freezing soils

Patterned ground is widespread in cold regions (1–8). Distinct sorted circles (1, 2, 5), stripes (1, 3), and labyrinths (5, 9), ranging in scale from a few centimeters to several meters, form during repeated freeze–thaw cycles as stones in the soil segregate according to size due to complex interactions among water and heat transport processes (10–13). However, stone patterns can evolve over thousands of years or more in the field (14, 15), making it difficult to determine their spatiotemporal behavior (see Fig. 1 and *SI Appendix*, Supporting Information Text S1 for more details). As a result, the fundamental physical principle underlying the phenomena and the quantitative characterization of the self-organization process remain unclear. Aside from creating stunning nonbiologic patterns in the natural world, the phenomenon merits close attention as it manifests soil processes important in carbon cycling in permafrost regions (5, 16, 17), which both affect and are affected by the rapid current warming in the Arctic, and it constitutes an extreme natural example of self-organization in excited granular materials (18–20).

Phase separation has in the past decades become a central physical principle for self-organized patterning in cell structure (21, 22), gravitational fluid (23, 24), active matter (18, 25–28), and ecological systems (29–31). Herein, we suggest that the principle leads to insights into pattern formation in geomorphic systems. It is important to note that it is distinct from the principle at the core of sophisticated phase-field models, which arise from regularized partial differential equations designed to solve moving boundary problems (32, 33), such as solidification fronts (34, 35), fracture (36, 37), and so on. The concentration-dependent movement feedback that leads to the spatial aggregation and dispersion of particles resulting in diverse patterns is central to the phase separation principle underlying our models. It contrasts with classical models with scale-dependent feedbacks; these include models using the foundational and widely applied Turing principle (see refs. 38 and 39 for details) and diverse other models, including those of systems in which organisms attach themselves providing positive feedback to aggregate at a small scale while creating negative feedback at a large scale, and of spatial patterns that form in near solidification fronts (35, 40–42). When a binary mixture, such as stones and soils, is subjected to periodic external forcing, for example, freeze–thaw cycles or cyclic vibrations, particles autogenically separate and commonly form distinct spatial patterns. This self-organization is similar to the well-known phase separation of a mixed fluid into two phases, in which separation

Significance

Self-organization is increasingly recognized as fundamental to pattern formation in geomorphology. Relative to other fields, however, underlying mechanisms have received little attention from theoreticians. Here, we introduce phase separation theory to study the formation of sorted patterned ground in cold regions; "sorted" refers to the segregation of soil and stones due to feedbacks between stone concentration and recurring ice growth. Using detailed measurements of the concentration of stones in soil and their displacements, we demonstrate that phase separation accounts for the observed sorting and patterns. Our study highlights phase separation theory as a source of important insight into studying ground patterns in cold regions and their potential value in signaling important changes in ground conditions with the warming climate.

Author contributions: A.L., N.M., and Q.-X.L. designed research; A.L., N.M., and Q.-X.L. performed research; Z.G. and N.G. contributed new reagents/analytic tools; F.N., J.C., Z.G., W.H., and D.L. analyzed data; A.L., N.M., B.H., J.v.d.K., N.G., and Q.-X.L. wrote the paper; F.N., B.H., and N.G. explained the data and results; and J.v.d.K. and Q.-X.L. wrote the codes.

The authors declare no competing interest.

This article is a PNAS Direct Submission.

This open access article is distributed under Creative Commons Attribution-NonCommercial-NoDerivatives License 4.0 (CC BY-NC-ND).

[1]To whom correspondence may be addressed. Email: liuqx315@gmail.com.

This article contains supporting information online at https://www.pnas.org/lookup/suppl/doi:10.1073/pnas.2110670118/-/DCSupplemental.

Published September 30, 2021.

Downloaded by Nigel D. Goldenfeld on October 3, 2021

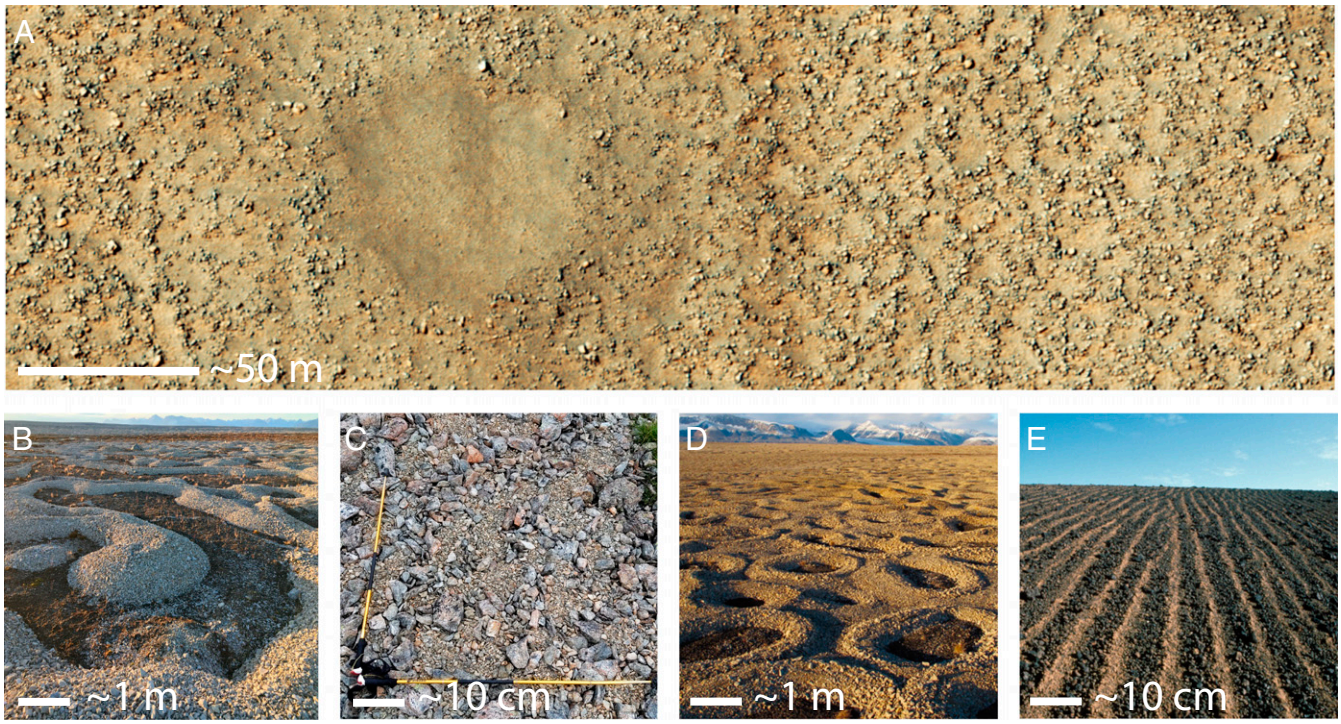

Fig. 1. Sorted patterned ground on Earth and Mars. Note range of length scales. (*A*) High Resolution Imaging Science Experiment (HiRISE) (ESP_030222_1220) image of clusters of boulders southeast of the giant Hellas impact basin, Mars. Image credit: NASA/JPL/UArizona. (*B*) Labyrinths of stones in Svalbard, Norway. Image credit: B.H. (*C*) Polygons in the Swiss Alps. Image credit: N.M. (*D*) Circles in Svalbard, Norway. Image credit: B.H. (*E*) Stripes in Hawaii, USA. Image credit: B.H.

driven by minimum free energy results in distinct spatial regions (43–45). Here, we investigate patterned ground self-organization by examining the dynamics of stone movements in laboratory investigations. We show that phase separation is expected during repeated freeze–thaw cycles, and using two models, we demonstrate how the concentration-dependent movement of stones produces diverse spatial patterns.

Results

Laboratory Experiment. Using a laboratory experiment with wet soil subjected to freeze–thaw cycles (46, 47), we demonstrate small-scale (1 to 10 cm) pattern formation resulting from cyclic growth and decay of needle ice on the ground surface developing either on level or sloping surfaces of a 100 by 50 cm soil area (see Materials and Methods, and *SI Appendix*, Figs. S1–S3). Our experiments addressed two key factors controlling the formation of stone patterns: the fraction of the ground surface covered by stones (hereafter termed stone concentration) and the slope of the surface (*SI Appendix*, Table S1). Stone patterns developed from stones that were initially evenly distributed. Within the first five freeze–thaw cycles, small stone clusters form and progressively merge with adjacent ones (Movies S1–S3). Coarsening of stone clusters occurs (48, 49), and well-defined patterns are eventually generated (see Fig. 2*A* and *SI Appendix*, Fig. S4 for more information). On level ground, the patterns range from dispersed stone clusters to connected irregular labyrinth forms as the stone cover increases from 20 to 60%; isolated stone-free islands form where the initial stone concentration is high (reference Movies S1–S3). On inclined ground, as the slope increases from 5° to 7°, the stone patterns transition to stripe-like patterns aligned downslope; clear patterns did not form on steeper slopes (46).

Physical Mechanisms Underlying Patterned Formation. The stone patterns in our experimental system result from the interactions between stone concentration and the amount of needle ice that forms under the stones. Needle ice growth and subsequent collapse due to thawing are the direct drivers of stone motion (*SI Appendix*, Fig. S2). The horizontal transport of individual stones is stochastic and dependent on the length and curvature of the underlying ice needles and local stone concentration. Contrary to common assumption, much of this transport occurs during the freezing phase (Movies S4 and S9). The amount of needle ice that forms and the resulting stone motion in areas with low-stone concentration (sparse stone areas) exceed those in areas of high-stone concentration (dense stone areas) (*SI Appendix*, Fig. S2 *A–C*). This drives net lateral transport of stones toward areas with high-stone concentration and further increases the stone concentration there (*SI Appendix*, Fig. S5 and Movie S4). This positive feedback is further enhanced by the recently recognized tendency for ice needles to curve and to move stones they lift toward stone-rich areas (46, 47). On the other hand, high-stone concentrations reduce needle ice growth, needle ice curvature, and stone motion. This effect results in the stacking of stones in a direction perpendicular to the soil surface (Movie S4), rather than moving and dispersing them laterally, and hence creates a negative feedback to stone aggregation. On sloping ground, in addition to lateral sorting processes, downslope frost creep and toppling or sliding failures during thaw phases play important roles in net downslope displacement of stones, leading to elongated patterns oriented downslope (46). Together, these physical processes that drive stone movement and pattern formation are critically dependent on the spatial variation of stone concentration, as well as the cumulative stone displacements caused by needle ice growth and collapse.

The fact that the stochastic transport of stones depends on the local stone concentration and surface slope implies that their dynamics are nonlinear, potentially leading to pattern forming instabilities. The transport of stones is strictly mass conserving,

Downloaded by Nigel D. Goldenfeld on October 3, 2021

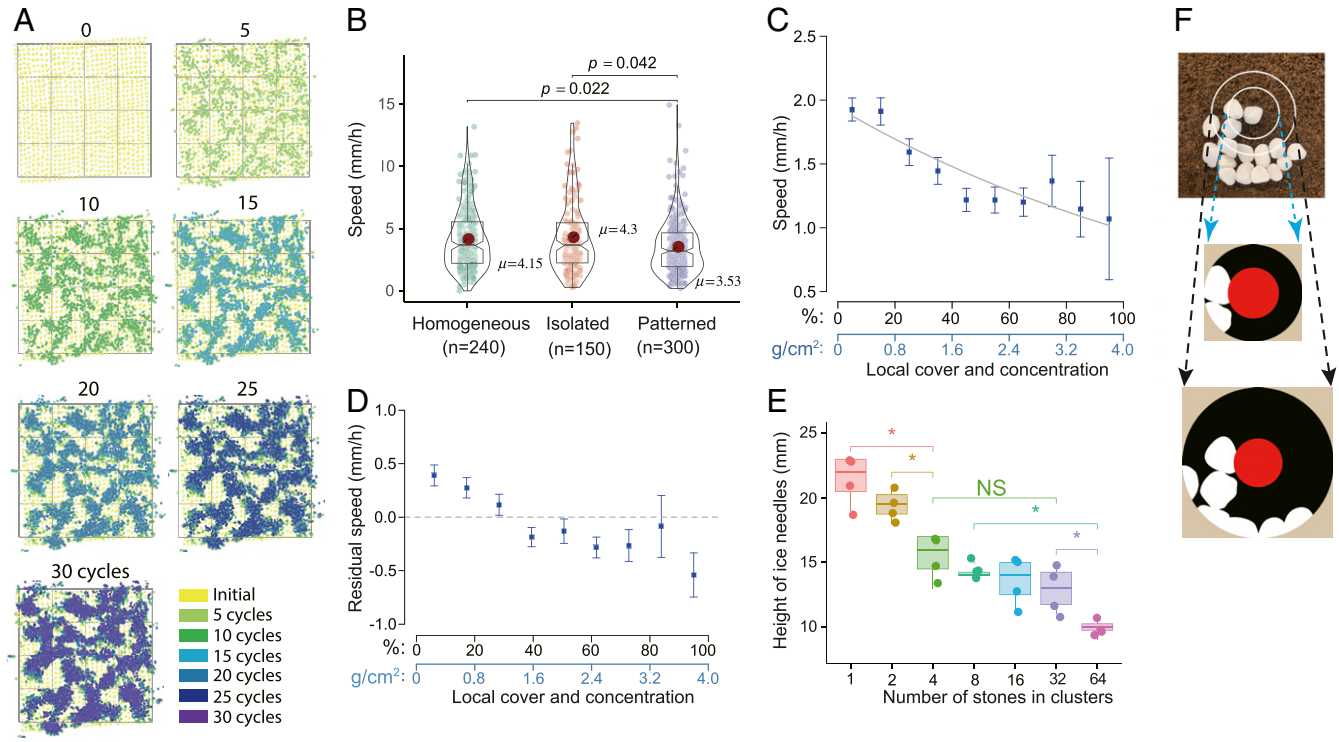

Fig. 2. Self-organization of stone patterns and stone motion in the laboratory. (*A*) Spatial pattern development starting from a uniform 30% stone cover through 30 freeze–thaw cycles. The panels cover an area ∼0.4 m on a side. (*B*) Box violin plots of the speed of individual stones for three configurations, homogeneous state at 80% cover (no patterns), isolated stones, and arrested stones (within patterns) at 40% cover (patterned), respectively. The boxplot spans the 25th to 75th percentiles. Red dots indicate mean values. The statistical analysis was implemented with Welch's one-way ANOVA, $F(2,356) = 6.61$, $P < 0.01$, and the significant levels were adjusted with the Benjamini–Hochberg method for comparisons among groups. (*C*) Relationship between stone speed and local stone concentration (within ∼3-cm radius, see *F*) during ∼30 freeze–thaw cycles. The solid line is the function $v(S) = v_0 e^{-\lambda S}$ with a decay rate of $\lambda = 0.85$, $P < 0.01$, and $n = 1854$ (reference *SI Appendix*, Table S2 for models' selection and statistical parameters). (*D*) Similar to *C*, the residual speed but removal of the effect of concentration beyond twofold radius. (*E*) Inverse relationship between the needle ice height and number of stones in clusters ($n = 4$ per treatment). The significance of changes among treatment clusters: $^*P < 0.05$, ,and "NS" for $P > 0.05$. Error bars represent one SD in *C*–*E*. (*F*) Schematic diagram shows the definition of the local cover and concentration for the center stone in the analyses of *C* and *D*. Reference Movies S1–S4 for sorted patterned ground and stone movement.

and pattern formation can arise either through nonlinearities arising from thermodynamics, as in phase separation in binary alloys (50), or from motility-induced phase separation (27, 28, 51). This latter possibility is clearly supported by our laboratory experiments that document how stones move as if self-propelled through their interaction with ice needles and the local stone concentration field around individual stones. In general, isolated stones move significantly faster than stones with close neighbors [Fig. 2*B*; $F_{welch}(2,357) = 6.61$, $P < 0.01$]. Our data analysis yields a strong negative relationship between stone speed and local stone concentration at multiple scales (Fig. 2 *C* and *D* and *SI Appendix*, Table S2); stones slow down when the surrounding stone concentration increases. This negative relationship is robust in terms of residual analysis, even when excluding the larger-scale interactions (*SI Appendix*, Fig. S6).

Phase Separation Implications for Patterned Ground Formation. We now consider two classes of models that quantify the relation between the stone speed $v(S(\boldsymbol{r}), H(\boldsymbol{r}))$, local stone concentration $S(\boldsymbol{r})$, and height of ice needles $H(\boldsymbol{r})$, where $\boldsymbol{r} = (x, y)$ represents position. As a first approximation, we assume that these effects can be separated so that $v(S,H) = v_H(H)v_S(S)$. This parametric velocity dependence on space implies that the dynamics of the stones will show important deviations from Fick's Law, as is known to occur in other systems, such as bacterial motion, where the effective mobility is concentration dependent (52). We represent the dependence of stone motion on concentration (Fig. 2*C*) as $v_S(S) = v_0 e^{-\lambda S}$ [this constitutes the core of Model 1 with $v_H(H) = 1$; see Fig. 3*A* and *SI Appendix*, Supporting Information Texts S2 and S3 for more information]. Experimental data also revealed a relationship between local stone concentration and H, the height of ice needles. H declines with increasing number of stones in clusters (groups of overlapped and constrained stones) from 1 up to 64 (Fig. 2*E*), showing that stone speed decreases with increasing concentration S and decreasing H. Thus, we assume that $v_H(H)$ is an increasing function of H and explore consequences of specific assumed forms for $v_H(H) = \beta H$ in Model 2 (Fig. 3 *B*, *Top*).

For both models, the change of spatial stone concentration with time obeys the law of conservation of mass, $\frac{\partial S}{\partial t} = -\nabla \cdot \boldsymbol{J}_v$, with a local stone concentration that is composed of gradients of S and H, along with rotationally invariant scalars of which the lowest order is $\nabla^2 S$. This results in the following:

$$\boldsymbol{J}_v = -\gamma v\left[v\nabla S + S\frac{\partial v}{\partial S}\nabla S + S\frac{\partial v}{\partial H}\nabla H\right] + \kappa\nabla\left(\nabla^2 S\right). \qquad [1]$$

Here, $\gamma = 1/\alpha d$, where α is the collision rate per stone that depends upon position and direction of motion (52), d is the spatial dimension (i.e., ref. 2), $\kappa > 0$ is the coefficient of potential energy forces (equivalent to the dispersal coefficient by a unit stone at a nonlocal scale) (52), and $\sqrt{\kappa}$ is the characteristic width of the mobile convergent front of the low- and high-concentration phases. In principle, there could be a higher-order term in H, but this is neglected

Downloaded by Nigel D. Goldenfeld on October 3, 2021

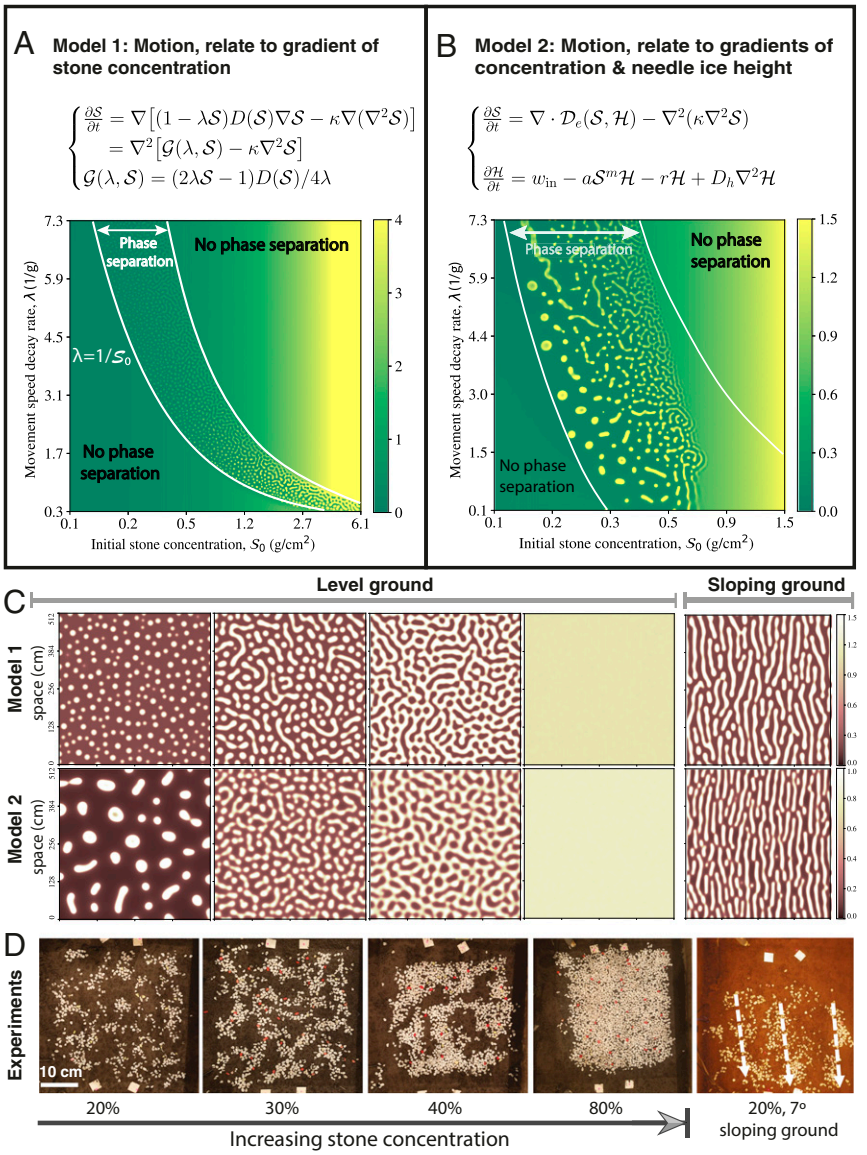

Fig. 3. Phase separation and the diversity of self-organized stone patterns. (*A* and *B*) Phase diagrams illustrate the dependence of pattern formation for both models (*Top*) on stone concentration and speed decay rate (λ) and define the regions in which the phase separation switches from the one- to two-phase regimes (*Bottom*): stone-poor and -rich phases. Each point (x, y) represents a parameter set ($S_0 = x$, $\lambda = y$) for the model equations. The theoretical predictions (white lines) coincide with numerical results. (*C*) Simulated 2D stone patterns with increasing stone concentrations from 20 to 80% for both models. Numerical simulations were implemented using periodic boundary conditions with parameters $\lambda = 3.0$, $d = 2$, $\tau = 1.0$, and $v_0 = 2.02$ (reference *SI Appendix*, Table S3 for additional details). Islands transform to labyrinths and polygons with increasing stone concentration, and no pattern develops at high-stone concentration. Color bar represents stone concentration in units of g/cm^2. Spatial scale with 5.1 m. (*D*) Self-organized patterns formed in the laboratory within 240 to 360 h due to repeated freeze–thaw cycling with stones initially laid out evenly on the soil surface: islands (20% cover), labyrinths (30% cover), polygons (40% cover), homogeneous state (80% cover), and incipient stripes (20% cover on a sloping surface of 7°; white arrows show the general downslope direction) [reprinted with permission from ref. 46]. Reference Movies S5 and S6 for numerical simulations of Model 1 and 2, respectively.

here as the characteristic front width is likely to be much smaller than for S. The mobility of individual stones can be expressed by an effective diffusivity $D_e(S,H) = D(S,H)\nabla S + SD'(S,H)/2$, where $D(S,H) = \gamma v(S,H)^2$ in the models. To complete our description of the coupled needle ice stone system, we represent the negative feedback between the stone concentration and needle ice height by the following equation (Fig. 3 *A* and *B*):

$$\frac{\partial H}{\partial t} = w_{in} - aS^m H - rH + D_h\nabla^2 H. \qquad [2]$$

On the right-hand side, the first term w_{in} describes the water input in the soil. The second term describes the inhibitory effect of increasing stone concentration on needle ice growth; a and m are positive empirical coefficients, where m represents the sensitivity of ice growth to stone concentration ($m = 2$ is assumed here, because a linear coupling between S and H is ruled out by the upward curvature visible in Fig. 2*E* and *SI Appendix*, Fig. S1). r is the specific rate of loss of the H_2O (both water and ice) due to evaporation, and D_h is the diffusion coefficient representing the H_2O (both water and ice) transport processes during a freeze–thaw cycle. Eqs. **1** and **2** constitute a complete description of the system dynamics. The form of Eq. **1** is reminiscent of the equations governing phase separation in alloys and is expected to lead to pattern formation. To check this, we compared our experimental results with the two models of patterning resulting

Downloaded by Nigel D. Goldenfeld on October 3, 2021

from ice-induced stone displacements: one dependent on stone concentration only (Model 1, Fig. 3*A* and Movie S5), and the other also including explicitly the dependence on the height of ice needles (Model 2, Fig. 3*B* and Movie S6). Our models yield diverse spatial patterns, similar to those emerging under a range of experimental conditions (Fig. 3 *C* and *D*) and at various field sites (Fig. 1 *B*–*E*). They include well-defined stone islands, as well as stone circles, and labyrinths on level ground. There are two end members in our theoretical phase separation model: bare soil with no stones ($S \to 0$) and soil with the ground surface fully covered by stones ($S \to 100\%$). According to theory, these single-phase regions are bound by curves, $\lambda = 1/S_0$, so-called spinodal lines as shown in Fig. 3*A*. In the two-phase regions, both islands and labyrinthine patterns emerge in a finite concentration range. This theoretical phase separation boundary coincides with laboratory experiments, where regions of intermediate stone concentration separate distinctly into homogenous regions with either sparse or dense stones (Fig. 3 *C* and *D*). These results illustrate the important role of needle ice height in shaping the sorted patterns with different stone concentrations (Fig. 3*B* and *SI Appendix*, Fig. S10). In the experiments, the self-organization was pronounced, forming distinct stone patterns, including stone islands, labyrinths, or circles, which emerged after only 30 freeze–thaw cycles in experiments with initial stone concentration below S_c (ca. 60%). Above this critical value, only a few large clusters of stones formed (Fig. 3*D* and Movie S7). Note that the phase separation models also reproduced stripe-like patterns on sloping ground by incorporating downslope soil creep effects into the models (Fig. 3 *C* and *D*).

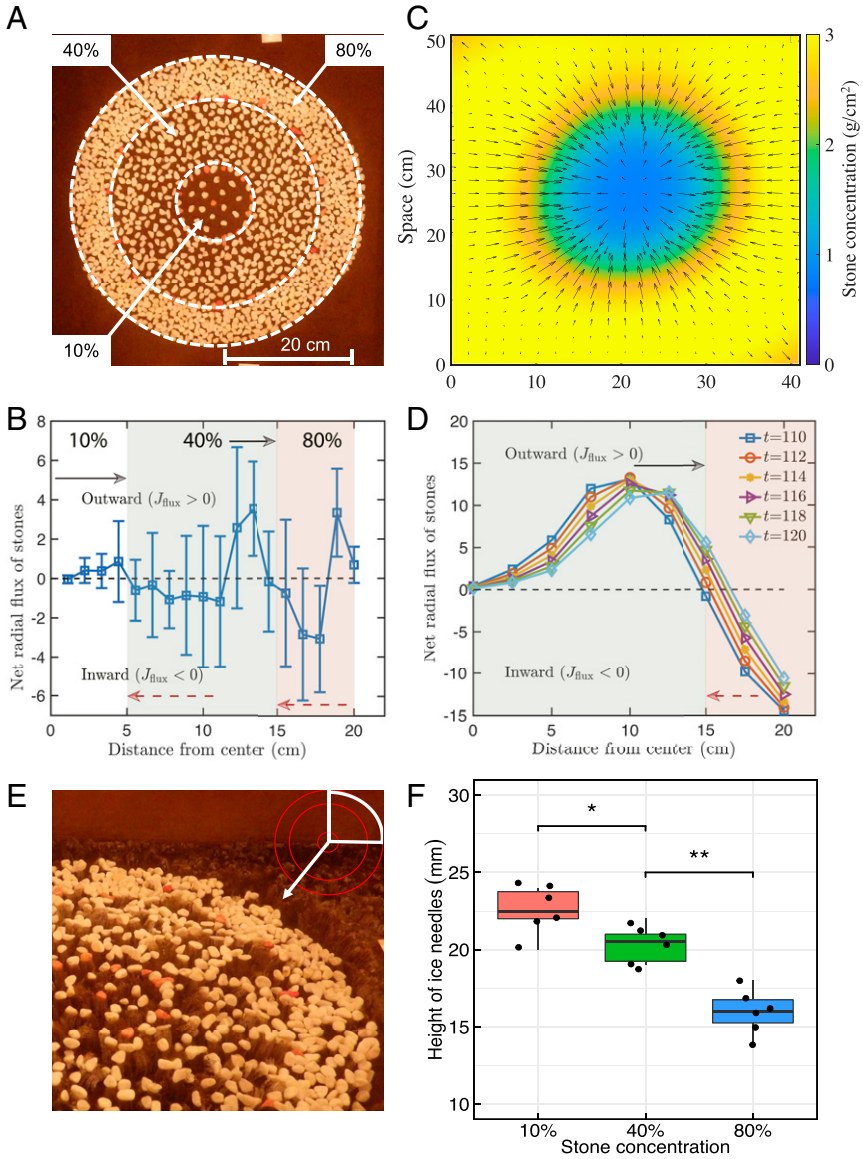

Fig. 4. Comparing experimental and theoretical results for well-defined, triple concentration patterns. (*A*) Vertical view of initial arrangement of stones in concentric rings of increasing stone concentration away from the center. (*B*) Observed net radial flux of stones, positive for outward and negative for inward. (*C*) Stone displacement field from phase separation Model 1 with $\lambda = 0.85$. (*D*) Stones diverge from the stone-poor central domain and move inward from the inner side of stone-rich peripheral domain. (*E*) Radial decrease in needle ice height with increasing stone concentration during first freezing period. Inset shows the area photograph. (*F*) Box plots showing needle ice height in the three concentric 10, 40, and 80% stone domains shown in *A*. Boxes extend from the lower to upper quartile values of the data. Horizontal lines mark the median heights. Comparisons are as follows: $*P < 0.05$ and $**P < 0.01$. Reference Movies S8 and S9 for experimental details.

Downloaded by Nigel D. Goldenfeld on October 3, 2021

As is well-known, phase separation initially arises from a linear instability in which particles diffuse from low concentration to high concentration, that is, opposite to Fick's Law, until nonlinearities overwhelm the aggregation process, leading to pattern restabilization through scale-invariant dynamics (53). To test these predictions and the expected relationship between stone velocity and concentration in phase separation models, we conducted an experiment with three domains with different initial stone concentrations as shown in Fig. 4 (see Materials and Methods and *SI Appendix*, Fig. S7). The velocity fields in both the model and experimental data coincide with one another: velocities shifting from radially outward to inward with increasing distance from the center (Fig. 4 *B*–*D*). The net radial flux is outward for lower concentration, but it is inward for high concentration. It is noteworthy that two clear dips appear at the interfaces between stone-poor and -rich domains. Interfacial phenomena are strongly implicated in coarsening dynamics for phase separation described by the quartic gradient term of Eq. **1**. Furthermore, as the stone concentration increases from 10 to 80%, needle ice crystals decrease in both height and curvature (Fig. 4 *E* and *F*, respectively), confirming the negative feedbacks between stone concentration and motion and providing further impetus for extending the phase separation model with a single variable (Model 1) to one (Model 2) with two variables. Overall, our results indicate that the phase separation models capture the key elements of self-organization in wet soils undergoing diurnal freeze and thaw cycles.

Scale Invariance and Self-Similar Dynamics of Patterns. To determine whether our data displayed nonlinear restabilization and dynamic self-similarity expected from the models, we analyzed all images in each experiment (e.g., ∼2,160 images for 30 freeze–thaw cycles in an experiment with 40% stone cover) and characterized the length scale of the observed patterns using two-dimensional (2D) Fourier analysis (54) (power spectra were derived using a square, moving window method). We calculated the temporal evolution of the dominant wavelengths for level and sloping ground surfaces (*SI Appendix*, Fig. S8). The wavelengths in the early phase of the experiments are in quantitative agreement with the simulations. They increase considerably and nonlinearly in the first 180 h within 15 freeze–thaw cycles; subsequently, the patterns stabilize (Fig. 5 *A* and *B*). Importantly, the models qualitatively account for this early coarsening behavior, which is robust and independent of initial stone concentration and surface inclination. For sloping ground, experimental results coincide with the $t^{1/3}$ scaling law that is standard in phase separation models (22, 29) during the first 180 h (∼15 freeze–thaw cycles; Fig. 5*A* and Table 1). In contrast, for level ground, experiments reveal a $t^{0.23}$ scaling law (Fig. 5*B* and Table 1). This type of scaling law agrees with the results of a quite different grain-scale model developed by Kessler et al. (2, 10) who focused on seasonal frost heave and subsurface ice growth as formative mechanisms for the larger scale (∼2- to 4-m diameter) patterned ground.

It is noteworthy that the relatively fast coarsening behavior on sloping ground can be attributed to the more directional movement with a bias downslope than that random stone movement in level scenarios (*SI Appendix*, Fig. S5), as well as the progressive elimination of complementary stripe defects, so-called stripe termination pairs (3). A similar phenomenon occurs in other systems in which there are long-range interactions, such as in block copolymers that only exhibit microphase separation at long times. However, at short times, even these systems exhibit phase separations, although the exponent describing the growing length scale is frequently found to be of order 1/4, at least when the interface width is not very small with respect to the domain size (45). Here, the oriented movement can result in overlapping stones on sloping ground, whereas level ground display quasiconservation (*SI Appendix*, Fig. S9). The deviation from the scaling laws after 15 freeze–thaw cycles presumably occurs because the models do not consider other geomorphic processes (55). This slow down and 0.25 power-law behaviors could in principle be captured with an additional term that describes interfacial dynamics, such as the celebrated Kardar–Parisi–Zhang dynamics (32, 45, 56, 57).

To quantify the emergent length scales (58) more precisely, we calculated the dynamic structure factor $S(q,t)$, where q is the modulus of the wave vector, that is, the Fourier variable conjugate to $\boldsymbol{r}$. At large q, the functional form of $S(q,t)$ is determined by the boundaries between phases and in 2D is expected to lead to a variant of Porod's Law, where $S(q,t) \sim q^{-3}$ (59). Both model

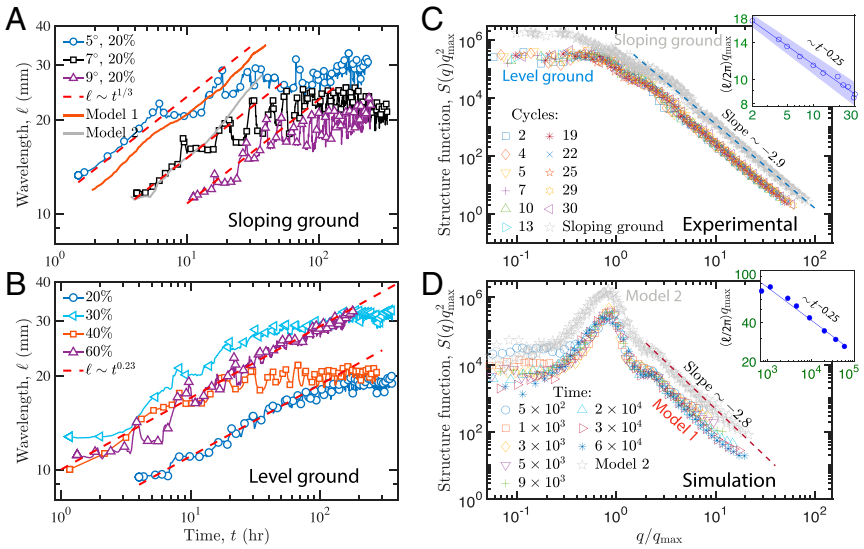

Fig. 5. Scaling behavior of the pattern coarsening from experiments and simulations. (*A* and *B*) Temporal evolution of dominant pattern wavelength on sloping and level ground. Note, the datasets are offset from one another for graphical clarity. Experimental data (colored solid lines with symbols) and numerical simulations with both phase separation models (solid lines). The dashed lines fit the experimental data with a power law at early stages. (*C* and *D*) Scaling behavior of the self-organized patterned ground from experiments and models. The rescaled structure function $S(q)$, as a function of wavenumber q/q_m, $q_m = \int qS(q)dq / \int S(q)dq$, versus the number of freeze–thaw cycles for experiments and simulations (see Materials and Methods for details). (*Insets*) The scaling of dominant wavenumbers plotted against the freeze–thaw cycles.

Downloaded by Nigel D. Goldenfeld on October 3, 2021

Table 1. Statistical properties of coarsening dynamics on experimental evolution at early stages

Experiment	Exponent*	SD	*P* value	R^2	*n*
Sloping ground	0.34	±0.010	<0.0001	0.78	3
Level ground	0.23	±0.012	<0.0001	0.87	4

Note that the nonlinear regression model was used to obtain the exponent with "fitnlm" function in MATLAB 2020b. *n* indicates the independent experimental replicates.

and experiment follow this universal trend. Furthermore, the rescaled structure factors collapse to form a master line when $S(q)q_{\max}^2$ is plotted versus q/q_{max}, where q_{max} is the time-dependent wavenumber corresponding to the width of spatial patterns from $S(q,t)$, indicating that numerical simulations and experiments are undergoing the same coarsening process (Fig. 5 *C* and *D*). The reason that $S(q,t)$ does not vanish as q tends to zero is that the stones overlap so that effectively in 2D the global conservation of mass does not hold. The time evolution of q_{max} is shown in the insets of Fig. 5 *C* and *D*. Whereas the scaling collapse reported above is expected in any phase separation process with a single, emergent length scale, the time dependence of the length scale reflects finite-time and finite-size effects and need not be power law. In theoretical studies of motility-induced phase separation, the exponents have also been found to be in the range 0.2 to 0.3, possibly indicative of slow crossover to a value 1/3. The observation of these dynamic scaling laws in our experiments and models is an example of motility-induced, sorted patterned ground formation going beyond phase separation in the active matter (24, 28).

Discussion

Two models currently exist for the origin of patterned ground; both are based on grain-scale numerical simulations. In the first, Werner and Hallet (3) suggested that differential growth of needle ice (between soil domains having different elevations and different abundances of stones) produced stone stripes with a typical spacing of ∼0.1 m. In the second, Kessler and Werner (2) proposed that a diversity of forms of meter-scale patterned ground emerge spontaneously from two feedback mechanisms associated with subsurface ice growth (lateral sorting and stone domain squeezing during ground ice freeze–thaw). These seminal models have been very instructive, but they have yet to be thoroughly tested or validated. Here, we took quite a different approach. Starting with unprecedented results from laboratory experiments, we developed a theoretical foundation, building on recent phase separation studies but with a modification that arises from the active or nonequilibrium nature of the needle ice–driving force. Our phase separation model provides a coherent explanation of the early stages of sorted patterned ground but does not aim to be a numerically predictive model of its long-term evolution (2, 3). By modeling the feedback between the amount of needle ice and the stone concentration, we reproduced the field-observed diversity of stone patterns, including stone circles, labyrinthine patterns, and islands on level ground. Incipient stripe-like patterns developed on sloping ground, but the formation of very well-defined regular stripes in laboratory may require a much larger experimental apparatus and larger numbers of freeze–thaw cycles.

Theoretically, we remark that the pattern formation mechanisms discussed here involve large-scale instabilities throughout the region of interest and are of a somewhat different character than other geophysical pattern formation phenomena that arise from front propagation. For these phenomena, such as crack formation in basalt columns (36, 37), advanced moving boundary methods can be used, for example, using so-called phase-field models (33, 34).

The pattern forming mechanisms driving the phase separation process in Arctic sorted patterns results from cyclic freezing and thawing. Because of that, changes in rock pattern formations may be indicative of changes in freezing conditions, pointing to permanent thawing in areas where patterns are observed to be lost. Our results support these predictable arguments that sorted patterned ground are not only by themselves sole local movement processes (Fig. 3*A*) but also dependent on the feedback effect of needle ice on movement speed (Fig. 3*B* and *SI Appendix*, Fig. S10). Hence, changes in the characteristics of rock patterns may be a crucial first sign of local climate change impacts, pointing at potential future soil loss. This may be observed on Arctic regions on earth, but changes in rock pattern formations may equally be indicative of changing conditions on Mars or other planets and could in the future be used to study temperature changes as well as the dynamics of soil conditions with planetary studies.

Aside from its intriguing geometric regularity, patterned ground is important because it may provide valuable information about surface processes and conditions in remote or hostile regions where detailed observations or monitoring are difficult or impossible, both on Earth and beyond. For instance, changes in patterned ground may signal subsurface changes in the vast permafrost regions of the warming Arctic where instrumentation is extremely sparse at best (16). Visible changes in patterned ground could provide important clues about the release of greenhouse gases from the permafrost to the atmosphere (60). Novel types of patterned ground on Mars revealed in detail by the Curiosity rover are currently being studied to further understanding of the underlying processes and the clues they contain about energy and mass exchange between the atmosphere and lithosphere on our neighboring planet (61). Our mathematical description of the universal principles that govern pattern formation contributes to understanding the processes that shape ground surfaces found in cold regions and may help in identifying the impacts of global climate change on our own planet.

Materials and Methods

Sorted Patterned Ground Implementation in Laboratory. The laboratory experiments were implemented with the same procedures and environmental conditions but on level ground and sloping ground, respectively. We first conducted a series of experiments in the controlled cold room to simulate patterned ground formation on level ground conditions with 20, 30, 40, 60, and 80% stone concentration, being ∼648, 912, 1,226, 1,916, and 2,597 stone individuals, respectively. The second series of experiments targets patterns on sloping ground by changing gradient from 5 to 11% (ref. 46) (*SI Appendix*, Table S1). The height of needle ice, soil temperature, and moisture were recorded at 10-min intervals with two multichannel data acquisition systems in each experiment (46, 47). Once each experiment had finished, all images of the surface patterns from top and side view were connected to produce a video (Movies S1–S3 and S7).

Feedback Between Stone Clusters and the Height of Ice Needles. In addition to concentration-dependent movement determining the dynamics of self-organized patterns, the height of ice needles contributes a crucial role to stone movement and pattern evolution. To quantify the relationship between local stone concentration and height of ice needles, we manually measured the height of ice needles below stone clusters of 1, 2, 4, 8, 16, 32, and 64 individual stones of 4 to 8 mm in diameter, which were stacked into seven circles naturally corresponding to diameters of 0.5, 0.8, 1.5, 2.0, 3.0, 4.0, and 6.0 cm, respectively. In general, we found that the needle ice height is inversely proportional to the number stones of the clusters from 1 up to 64 and is consistent with the negative relationship between stone movement and the height of ice needles. We see the same general relationship between stone concentration and stone speed.

Real-Time Trajectory and Local, Concentration-Dependent Movement Analysis. To quantify the relationship between gradient in stone concentration and pattern formation, and how interactions between individual stones (clusters) determine pattern formation, we manually traced the movement of individual stones in successive images of our experiments and analyzed their characteristics in relation to gradient in concentration. All the movement trajectories of individual stones were recorded manually using the free software Fiji (https://imagej.net/Fiji/Cite, developed by the NIH) with the Track-Mate package (62).

Downloaded by Nigel D. Goldenfeld on October 3, 2021

We determined both the speed of and extent of stone concentration surrounding individual stones by extracting the specific stones as they moved from an isolated location toward the patterned inner and open areas (soil). The concentration of stones in the neighborhood of a tracked stone was estimated by measuring the fractional cover of the stones within the distances of 1.2-, 2.0-, 3.0-, 4.0-, 5.0-, 6.0-, 7.0-, 8.0-, and 9.0-fold of the diameter (see Fig. 2*F* for an example). These specific setups correspond to the spatial scales of about 12, 18, 24, 30, 42, 48, and 54 mm for stones with an ∼6-mm stone diameter. Following the methods proposed by van de Koppel and coauthors (63), images were converted to binary bitmaps indicating the presence or absence of stones using a custom-made MATLAB program. All circles were extracted from these bitmaps, with the tracked stones set at the center. The central circle of the onefold radius was excluded as it contains the tracked stone itself. To covert the cover estimates to concentration (as it is convenient to use continuum variables in the theoretical model), we precisely measured the local concentration of stones with 100% cover and their weight. Finally, we obtained the conversion factor of 4.0 in our laboratory experiments; that is, local stone concentration is about 4.0 g/cm^2 when the stone cover is 100%.

Statistical Analyses. A one-way ANOVA was used in R (64) to test whether speeds differ among stones in homogenous, isolated, and patterned scenarios. A Bonferroni correction was employed, and all *P* values below 0.05 were considered significant. Statistical details can be found in the main text and figures. A data point was considered an outlier if it was greater than the 75th quartile + (1.5 × interquartile range [IQR]) or lower than the 25th quartile − (1.5 × IQR). Furthermore, we analyzed the relation between local stone concentration and speed with a generalized linear model using hyperbolic and exponential functions, respectively. The best single-scale model as well as the two-scale multiple model were selected from all possible sets using Akaike's information criterion. The summary results of the movement relationships are listed in *SI Appendix*, Table S2. The two-scale multiple model shows that the negative feedback always occurs at the largest radius based on the *Z*-score test. This implies that a two-scale feedback relation is unrealistic for our self-organized patterned ground experiments. This was further confirmed by the correlation coefficient of changed spatial scales as shown in *SI Appendix*, Fig. S6, in which the experimental data revealed positive feedback even at the scale of ninefold the diameter.

Velocity Field and Radial Flux Analyses. To quantify feedback between stone concentration and displacement field, a triple stone concentration sorted annulus experiment had been designed. Inside diameters of outer, intermediate, and inner circles are 40, 30, and 10 cm, respectively. Out annulus is full with 80% stones, while intermediate annulus and inner circles are full with 40 and 10% stones. All the stones were placed on the surface of soil in the container and subjected to 20 freeze–thaw cycles with air temperature oscillating between −5 and 10 °C for 12 h in a cold room. We obtained the velocity fields with Particle Image by Velocimetry PIVLAB package (version 2.02) in MATLAB 2019a (65). Contrast limited adaptive histogram equalization was used to enhance contrast, and a high-pass method was used to filtrate out the low-frequency signal during preprocessing of the images. For the laboratory experimental images and simulated data, we defined the point with the minimum velocity within the circular patch as the center of radial direction. The displacement velocity was obtained with two consecutive snapshots. Furthermore, we calculated the amount of net radial flux at distance $\boldsymbol{r}$ with formula $J_{\text{flux}}(\boldsymbol{r}) = \oint_0^{2\pi} \boldsymbol{v}(\boldsymbol{r}, \varphi) d\varphi$.

Data Availability. The experimental data analyzed during this study are available in the manuscript and *SI Appendix* files. All custom-made simulation codes are available online at GitHub: https://github.com/liuqx315/Phase-separation-patterned-ground. All other study data are included in the article and/or supporting information.

ACKNOWLEDGMENTS. We thank Wei Lu, Haobo Yang, Binqi Liu, Luming Fang, and Yunya Wang for assistance with preliminary tracking of stone movement in images, Purba Chatterjee for critical comments, and Kang Zhang for pyOpenCL code assistance. This work was supported by the Second Tibetan Plateau Scientific Expedition and Research program (Grant No. 2019QZKK0905), Japan Society for the Promotion of Science KAKENHI Grant No. 20K01138, the National Natural Science Foundation of China (Grant Nos. 41801043, 41676084, and 32061143014), and the Strategic Priority Research Program of the Chinese Academy of Sciences (Grant No. XDA19070504). A.L. gladly acknowledges the postdoctoral scholarship from the China Scholarship Council for supporting this work.

1. A. L. Washburn, *Geocryology: A Survey of Periglacial Processes and Environments* (Wiley, 1980).
2. M. A. Kessler, B. T. Werner, Self-organization of sorted patterned ground. *Science* **299**, 380–383 (2003).
3. B. Werner, B. Hallet, Numerical simulation of self-organized stone stripes. *Nature* **361**, 142–145 (1993).
4. B. Hallet, Spatial self-organization in geomorphology: From periodic bedforms and patterned ground to scale-invariant topography. *Earth Sci. Rev.* **29**, 57–75 (1990).
5. B. Hallet, Stone circles: Form and soil kinematics. *Philos. Trans.- Royal Soc., Math. Phys. Eng. Sci.* **371**, 20120357 (2013).
6. A. Kääb, L. Girod, I. Berthling, Surface kinematics of periglacial sorted circles using structure-from-motion technology. *Cryosphere* **8**, 1041–1056 (2014).
7. S. Grab, Characteristics and palaeoenvironmental significance of relict sorted patterned ground, Drakensberg plateau, southern Africa. *Quat. Sci. Rev.* **21**, 1729–1744 (2002).
8. J. Aalto, S. Harrison, M. Luoto, Statistical modelling predicts almost complete loss of major periglacial processes in Northern Europe by 2100. *Nat. Commun.* **8**, 515 (2017).
9. C. K. Ballantyne, *Periglacial Geomorphology* (Wiley Blackwell, Hoboken, NJ, 2018).
10. M. Kessler, A. Murray, B. Werner, B. Hallet, A model for sorted circles as self-organized patterns. *J. Geophys. Res. Solid Earth* **106**, 13287–13306 (2001).
11. R. A. Peterson, W. B. Krantz, A mechanism for differential frost heave and its implications for patterned-ground formation. *J. Glaciol.* **49**, 69–80 (2003).
12. R. Peterson, W. Krantz, Differential frost heave model for patterned ground formation: Corroboration with observations along a North American arctic transect. *J. Geophys. Res. Biogeosci.* **113**, G03S04 (2008).
13. R. Ray, W. Krantz, T. Caine, R. Gunn, A model for sorted patterned-ground regularity. *J. Glaciol.* **29**, 317–337 (1983).
14. B. Hallet, S. Prestrud, Dynamics of periglacial sorted circles in western Spitsbergen. *Quat. Res.* **26**, 81–99 (1986).
15. J. S. Levy *et al.*, Surface boulder banding indicates Martian debris-covered glaciers formed over multiple glaciations. *Proc. Natl. Acad. Sci. U.S.A.* **118**, e2015971118 (2021).
16. B. K. Biskaborn *et al.*, Permafrost is warming at a global scale. *Nat. Commun.* **10**, 264 (2019).
17. R. C. Glade, M. M. Fratkin, M. Pouragha, A. Seiphoori, J. C. Rowland, Arctic soil patterns analogous to fluid instabilities. *Proc. Natl. Acad. Sci. U.S.A.* **118**, e2101255118 (2021).
18. J. Zhang, R. Alert, J. Yan, N. S. Wingreen, S. Granick, Active phase separation by turning towards regions of higher density. *Nat. Phys.* **17**, 961–967 (2021).
19. Z. Li *et al.*, Microscopic structure and dynamics study of granular segregation mechanism by cyclic shear. *Sci. Adv.* **7**, eabe8737 (2021).
20. S. W. Meier, D. A. Melani Barreiro, J. M. Ottino, R. M. Lueptow, Coarsening of granular segregation patterns in quasi-two-dimensional tumblers. *Nat. Phys.* **4**, 244–248 (2008).
21. A. Radja, E. M. Horsley, M. O. Lavrentovich, A. M. Sweeney, Pollen cell wall patterns form from modulated phases. *Cell* **176**, 856–868.e10 (2019).
22. A. Klosin *et al.*, Phase separation provides a mechanism to reduce noise in cells. *Science* **367**, 464–468 (2020).
23. M. Sato, I. Sumita, Experiments on gravitational phase separation of binary immiscible fluids. *J. Fluid Mech.* **591**, 289–319 (2007).
24. M. Tateno, H. Tanaka, Power-law coarsening in network-forming phase separation governed by mechanical relaxation. *Nat. Commun.* **12**, 912 (2021).
25. J. Agudo-Canalejo, R. Golestanian, Active phase separation in mixtures of chemically interacting particles. *Phys. Rev. Lett.* **123**, 018101 (2019).
26. S. Thutupalli, D. Geyer, R. Singh, R. Adhikari, H. A. Stone, Flow-induced phase separation of active particles is controlled by boundary conditions. *Proc. Natl. Acad. Sci. U.S.A.* **115**, 5403–5408 (2018).
27. M. E. Cates, D. Marenduzzo, I. Pagonabarraga, J. Tailleur, Arrested phase separation in reproducing bacteria creates a generic route to pattern formation. *Proc. Natl. Acad. Sci. U.S.A.* **107**, 11715–11720 (2010).
28. R.-Y. Dong, S. Granick, Reincarnations of the phase separation problem. *Nat. Commun.* **12**, 911 (2021).
29. Q.-X. Liu *et al.*, Phase separation explains a new class of self-organized spatial patterns in ecological systems. *Proc. Natl. Acad. Sci. U.S.A.* **110**, 11905–11910 (2013).
30. Q. X. Liu *et al.*, Phase separation driven by density-dependent movement: A novel mechanism for ecological patterns. *Phys. Life Rev.* **19**, 107–121 (2016).
31. E. Demir, Y. I. Yaman, M. Basaran, A. Kocabas, Dynamics of pattern formation and emergence of swarming in *Caenorhabditis elegans*. *eLife* **9**, e52781 (2020).
32. E. Ben-Jacob, N. Goldenfeld, J. S. Langer, G. Schön, Dynamics of interfacial pattern formation. *Phys. Rev. Lett.* **51**, 1930–1932 (1983).
33. E. Ben-Jacob, N. Goldenfeld, J. S. Langer, G. Schön, Boundary-layer model of pattern formation in solidification. *Physical Review A* **29**, 330–340 (1984).
34. K. Vetsigian, N. Goldenfeld, Computationally efficient phase-field models with interface kinetics. *Phys. Rev. E Stat. Nonlin. Soft Matter Phys.* **68**, 060601 (2003).
35. N. Provatas, M. Greenwood, B. Athreya, N. Goldenfeld, J. Dantzig, Multiscale modeling of solidification: Phase-field methods to adaptive mesh refinement. *Int. J. Mod. Phys. B* **19**, 4525–4565 (2005).
36. E. A. Jagla, Maturation of crack patterns. *Phys. Rev. E Stat. Nonlin. Soft Matter Phys.* **69**, 056212 (2004).

Downloaded by Nigel D. Goldenfeld on October 3, 2021

37. A. Karma, A. E. Lobkovsky, Unsteady crack motion and branching in a phase-field model of brittle fracture. *Phys. Rev. Lett.* **92**, 245510 (2004).
38. M. Rietkerk, J. van de Koppel, Regular pattern formation in real ecosystems. *Trends Ecol. Evol.* **23**, 169–175 (2008).
39. A. M. Turing, The chemical basis of morphogenesis. *Philos. Trans. R. Soc. Lond. B Biol. Sci.* **237**, 37–72 (1952).
40. I. Eisenman, J. S. Wettlaufer, Nonlinear threshold behavior during the loss of Arctic sea ice. *Proc. Natl. Acad. Sci. U.S.A.* **106**, 28–32 (2009).
41. D. L. Feltham, N. Untersteiner, J. S. Wettlaufer, M. G. Worster, Sea ice is a mushy layer. *Geophys. Res. Lett.* **33**, L14501 (2006).
42. E. Ben-Jacob, N. Goldenfeld, B. G. Kotliar, J. S. Langer, Pattern selection in dendritic solidification. *Phys. Rev. Lett.* **53**, 2110–2113 (1984).
43. J. W. Cahn, J. E. Hilliard, Free energy of a nonuniform system. I. Interfacial free energy. *J. Chem. Phys.* **28**, 258–267 (1958).
44. A. Shinozaki, Y. Oono, Spinodal decomposition in 3-space. *Phys. Rev. E Stat. Phys. Plasmas Fluids Relat. Interdiscip. Topics* **48**, 2622–2654 (1993).
45. F. Liu, N. Goldenfeld, Dynamics of phase separation in block copolymer melts. *Phys. Rev. A Gen. Phys.* **39**, 4805–4810 (1989).
46. A. Li, N. Matsuoka, F. Niu, Frost sorting on slopes by needle ice: A laboratory simulation on the effect of slope gradient. *Earth Surf. Process. Landf.* **43**, 685–694 (2018).
47. C. Yamagishi, N. Matsuoka, Laboratory frost sorting by needle ice: A pilot experiment on the effects of stone size and extent of surface stone cover. *Earth Surf. Process. Landf.* **40**, 502–511 (2015).
48. T. Mullin, Coarsening of self-organized clusters in binary mixtures of particles. *Phys. Rev. Lett.* **84**, 4741–4744 (2000).
49. P. M. Reis, T. Mullin, Granular segregation as a critical phenomenon. *Phys. Rev. Lett.* **89**, 244301 (2002).
50. M. Park, C. A. Schuh, Accelerated sintering in phase-separating nanostructured alloys. *Nat. Commun.* **6**, 6858 (2015).
51. J. Tailleur, M. E. Cates, Statistical mechanics of interacting run-and-tumble bacteria. *Phys. Rev. Lett.* **100**, 218103 (2008).
52. M. J. Schnitzer, Theory of continuum random walks and application to chemotaxis. *Phys. Rev. E Stat. Phys. Plasmas Fluids Relat. Interdiscip. Topics* **48**, 2553–2568 (1993).
53. I. M. Lifshitz, V. V. Slyozov, The kinetics of precipitation from supersaturated solid solutions. *J. Phys. Chem. Solids* **19**, 35–50 (1961).
54. G. G. Penny, K. E. Daniels, S. E. Thompson, Local properties of patterned vegetation: Quantifying endogenous and exogenous effects. *Philos. Trans.- Royal Soc., Math. Phys. Eng. Sci.* **371**, 20120359 (2013).
55. P. S. Dodds, D. H. Rothman, Scaling, universality, and geomorphology. *Annu. Rev. Earth Planet. Sci.* **28**, 571–610 (2000).
56. R. Wittkowski *et al*., Scalar φ4 field theory for active-particle phase separation. *Nat. Commun.* **5**, 4351 (2014).
57. M. Kardar, G. Parisi, Y.-C. Zhang, Dynamic scaling of growing interfaces. *Phys. Rev. Lett.* **56**, 889–892 (1986).
58. L. McNally *et al*., Killing by Type VI secretion drives genetic phase separation and correlates with increased cooperation. *Nat. Commun.* **8**, 14371 (2017).
59. A. Shinozaki, Y. Oono, Asymptotic form factor for spinodal decomposition in three-space. *Phys. Rev. Lett.* **66**, 173–176 (1991).
60. A. K. Liljedahl *et al*., Pan-Arctic ice-wedge degradation in warming permafrost and its influence on tundra hydrology. *Nat. Geosci.* **9**, 312–318 (2016).
61. R. Sletten, B. Hallet, N. Mangold, A. G. Fairén, R. Sullivan Jr, "Distinct small-scale (0.1 to 1 m) regolith features suggest regolith activity and provide clues about the bedrock at Glen Torridon, Gale Crater, Mars" in AGU Fall Meeting Abstracts, (2019) pp. P31A–3429. https://ui.adsabs.harvard.edu/abs/2019AGUFM.P31A3429S.
62. J. Schindelin *et al*., Fiji: An open-source platform for biological-image analysis. *Nat. Methods* **9**, 676–682 (2012).
63. J. van de Koppel *et al*., Experimental evidence for spatial self-organization and its emergent effects in mussel bed ecosystems. *Science* **322**, 739–742 (2008).
64. I. Patil, Visualizations with statistical details: The 'ggstatsplot' approach. *J. Open Source Softw.* **6**, 3167 (2021).
65. W. Thielicke, E. J. Stamhuis, PIVlab—Towards user-friendly, affordable and accurate digital particle image velocimetry in MATLAB. *J. Open Res. Softw.* **2**, 30 (2014).

Downloaded by Nigel D. Goldenfeld on October 3, 2021

PNAS
www.pnas.org

Supplementary Information for

Ice needles weave patterns of stones in freezing landscapes

Anyuan Li, Norikazu Matsuoka, Fujun Niu, Jing Chen, Zhenpeng Ge, Wensi Hu, Desheng Li, Bernard Hallet, Johan van de Koppel, Nigel Goldenfeld, Quan-Xing Liu*

***Corresponding Quan-Xing Liu.**
E-mail: qxliu@sklec.ecnu.edu.cn

This PDF file includes:

Other supplementary materials for this manuscript include the following:

Supporting Information Text

Contents

S1. Motivation and background on patterned ground

Patterned ground ranging from decimeter- to meter-scale spatial wavelengths is a common morphological feature found in many cold and periglacial environments (1–22) and see *Supplementary information* (SI) Table S4 for more detailed information all over the world. It consists of mostly symmetrical geometries, such as circles, stripes, nets, and labyrinths, displaying across the Earth surface. Most research on patterned ground has involved field studies of the processes responsible for the characteristics of present-day patterns, and their feedbacks to climate change (1–3). Several studies focus on patterns origins and development, where patterned ground is ascribed to frost sorting (23–25), frost cracking (23), upfreezing (26), soil moisture flux (27) and wind action (4, 5). Earlier numerical models suggest that water-soil convection (27) controls the formation of observed patterned ground. Although these numerical models can reproduce sorted stone circles or stripes, they cannot provide full physical-based mechanisms for explaining the origin and evolution of these observed patterns. Kessler and Werner (2003) suggested that typical patterned grounds along a broad range of external environments form by self-organization processes (28). Based on the concept of self-organization, they developed a comprehensive model of patterned ground that successfully predicted pattern formation and transitions between different morphologies under different external conditions (slope and stone concentration). The formation of district patterns is controlled by three processes: lateral sorting, squeezing, and slope gradient. Although the model is powerful and useful for explaining observed self-organized patterned ground, experiment or field evidence to support this theory is still lacking. Hitherto, the explicit articulation of controlling rules that underlie the self-organization is missing (29). In this *Supplementary Information*, we take a step to providing a

detailed analysis of this problem through both controlled laboratory experiments and quantitative modeling.

S2. Laboratory experimental setup and environment measurement

A schematic diagram of the experimental apparatus is shown in *SI Appendix*, Figure S1A. Patterned ground formation by stones ($\rho_p = 2.01 \pm 0.01 g/\mathrm{cm}^3$) was studied in the laboratory with a 100 cm × 50 cm × 35 cm plastic container filled with volcanic soil ($\rho_s = 1.52 \pm 0.01 g/\mathrm{cm}^3$). The experimental soil was excavated at the campus of University of Tsukuba, Japan, where needle ice widely grew in winter (*SI Appendix*, Figure S1 C–E). The soil texture was a natural frost-susceptible mixture with 50% sand, 27% silt and 23% clay by weight after remove contaminates with a 2 mm mesh sieve. The entire soil was near-saturated by the sprinkling of water slowly from the top surface and allowing it to settle for ∼24 hours to homogenize moisture content, which ensured that the spatial distribution of soil moisture was homogeneous before experiments.

The whole container was wrapped with a heat-insulated foam board (∼10 cm thickness) on the sides (*SI Appendix*, Figure S1E). The container was subjected to 20 – 40 freeze-thaw cycles with air temperature oscillating between –5 °C and 10 °C in 12 hours in a cold room which was found to easily cause intensive needle ice activity (24, 25) (*SI Appendix*, Figure S1B). We began each experiment after cooling the container at 2 °C for ∼24 hours. Subsequently, the initial temperature allowed to reach ∼5 °C. As a natural clast simulant, white commercial stones 4 – 8 mm in diameter were used. They were laid-out at quasi-equal spacing on the volcanic soil surface over a square of 40 cm × 40 cm. The amounts of stones used were always such that a shallow layer regime was maintained, with layer height ranged from 4.2 ± 0.1 mm (at 20% concentration with 1 layer) to 6.3 ± 0.1 mm (at 80% concentration with ∼1.5 layers).

The growth and decay of needle ice was measured at 10-minute intervals on a 2.5 cm × 2.5 cm grid using a laser displacement sensor (IL030, Keyence, Japan). Temperature sensors (K-type thermocouples) were imbedded into soil at $0, 2, 5, 10$ and 15 cm depths respectively. Four thermo-hydro sensors (5TE, Decagon, USA) were used to monitor the soil moisture content inside the container at $2, 5, 10, 15$ cm depths. These soil moisture measurements corresponded closely with those measured with thermocouples at the same depths. All temperature and soil moisture data were automatically recorded at 10-minute intervals in two data acquisition system (NR-600, Keyence, Japan and Em50, Decagon, USA). Manual tests of the actual needle ice height below the stone clusters were not performed during the experiment to avoid artificial disturbance, but it was done during additional freezing (31th freezing) when an experimental run had finished. All movements of the pebbles and development of patterned ground were recorded by taking an image at 10-minute intervals using two time-lapse cameras, one was positioned about 50 cm above the soil central surface (arena) and the other was placed about 10 cm outside the container (*SI Appendix*, Figure S1A). For each experiment, we have carefully collected camera image data, from which we have subsequently produced movies of patterns evolution. We randomly selected several stones as markers (painted red or yellow) and manually tracked their positions by using a free software Fiji (https://imagej.net/Fiji/Cite, developed by National Institutes of Health) (30) for mapping trajectories in two-dimensional space. We cleaned the pebbles of attached soil using a syringe filled with 25 ml water regularly during the warming period. Note that no external perturbations were applied and the initial ground was essentially uniform in terms of texture and soil moisture content, and the ground surface was effectively planar for all experiments.

S3. Theoretical models of sorted patterned ground

In this section, we develop theoretical models to study the influence of concentration-dependent speed on phase separation of self-organized stones' patterns. In subsection S3.1, we first give a qualitative relationship between local stone concentration and their movement speed. Subsequently, we develop a simple mesoscopic model of phase separation based on the interaction between stones and the height of ice needles in subsection S3.2. We use the term "*phase separation*" to denote the evolution of patterns with a bimodal distribution of the stone concentration field in space. The separation is the process of an initially uniform state developing such a concentration pattern, similar to the patterns observed during phase separation in materials science. In fact, this analogy may not be superficial: mathematical similarities between the stone patterns and the phase separation patterns in materials science naturally arise as shown below.

S3.1. Theoretical model description. Our proposed phase separation models (Figure 3A in main text) capture interactions among stones and the relationships between the movement speed and local stone concentration. The details of concentration-dependent movement determine the emergence of self-organized patterns in our experiments as were shown in our main text for different stone covers (Figure 3D). In our models (see *SI Appendix*, Table S3 for definitions of its variables and parameters), $S(\boldsymbol{r})$ (here $\boldsymbol{r} = (x, y)$) describes the local concentration of stones. The stone speed observed experimentally, is well approximated as

$$v(S) = v_0 \exp(-\lambda S). \qquad [S3.1]$$

For simplicity, here, we have assumed that stone concentration is the only property affecting stone speed and neglected other potential influences. The experiments are well-enough resolved to extract the local stone concentration field, in a similar way to our previous method on mussel beds (31). However, the stones are moved also by needle ice clusters, and themselves influence the height of needle ice clusters. This interplay – plays a crucial role in stone mobility in two ways, and is a core conceptual framework in our work. First, thick needle ice clusters promote stone speed, and secondly, thick clusters are limited to low stone concentration areas as evidenced by our experiments. Therefore, both the local stone concentration and the local height of ice needles into determine the stone speed, so that more generally, the velocity in Eq. (S3.1) becomes as function $v(S, H)$, where H depicts height of ice needles.

We shall describe the above two physical processes and the resulting self-organized patterns as a binary mixture of needle ice and stones, with the stone concentration playing the important role of the concentration of one of the components in a binary allow in the appropriate phase field equation. As a result, we will see that our experimental stone systems display many of the features of phase separation dynamics (32).

S3.2. Deterministic models. To develop our phase separation framework, we first analyze a specific model of mobile stones whose speed depends directly on local stone concentration. Here the stones can interact locally in various ways, ranging from steric collisions to lateral squeezing (28) and random diffusion on soil surface due to needle ice bending in random direction below each individual stone (*SI Appendix*, Figure S2). Thus, the former processes lead to aggregation, locally increasing stone concentration. We focus on the net effect of all such interactions on stone speed $v(S, H)$, which decreased with increased concentration S, and decreased height of ice needles H, i.e. $\partial_S v(S, H) < 0$ and $\partial_H v(S, H) > 0$ (*SI Appendix*, Figure S12). This dependence might include the local effect of

squeezing-collision and the positive feedbacks between the height of ice needles and stone speed, which cause aggregation, but does not include top-surface tension driven by gravity, such as slip and rotation during the thawing of needle ice (33).

We now derive coarse-grained continuum equations for the mean-field concentration of stones $S(\boldsymbol{r}, t)$ in a two-dimensional space, with a velocity-concentration relation of the generic form $v(S, H)$ fitted from our experimental data. At large scales in a uniform system, the motion of individual stone is characterized by a diffusivity equation of the coefficient,

$$D\left(S, H\right) = \gamma v(S, H)^2, \qquad \text{[S3.2]}$$

with $\gamma = 1/d\alpha$. Here α is the tumbling rate of stone trajectories without collision events, and d is the spatial dimensionality, as follows from earlier existing mathematical derivation ($d = 1$ for one dimension and $d = 2$ for two dimensions) (34, 35). In contrast to constant speed, a spatial nonuniform stone speed $v(S, H)$ also results in a local-drift flux in this case given by $\boldsymbol{J}_v = -\gamma v(S, H)\nabla[v(S, H)S]$ (35). In the case of concentration-dependent movement, the drift flux of stones gives:

$$\begin{aligned} \boldsymbol{J}_v &= -\gamma v \left[(v + S\frac{\partial v}{\partial S})\nabla S + S\frac{\partial v}{\partial H}\nabla H\right] \\ &= -\left[\underbrace{D(S, H)\nabla S + SD^{'}(S, H)/2}_{=D_e(S,H)}\right] = -D_e(S, H). \end{aligned} \qquad \text{[S3.3]}$$

Note that the velocity-concentration relation $v(S, H)$ is a function of S and H, both of which are a function of spatial location $\boldsymbol{r}$. In the last step we have expanded the term $\nabla[v(S, H)S]$ and we suppressed the explicit dependence of the speed on the concentration of stones and the height of ice needles for notational simplicity.

The change of spatial stone distribution is expressed by the above drift fluxes and mass conservation processes as $\frac{\partial S}{\partial t} = -\nabla \cdot \boldsymbol{J}_v$. We can now combine the net flux of stones in equation (S3.3) with the effective surface tension caused by the gravitational potential to define the general conservation dynamics for self-organized stones' patterns by

$$\frac{\partial S}{\partial t} = \nabla \cdot \left[D_e\left(S, H\right)\right] - \nabla^2 \cdot \left[\kappa \nabla^2 S\right]. \qquad \text{[S3.4]}$$

Here D_e is referred to as the effective diffusivity, (κ is the coefficient of potential energy forces (equivalent to the dispersal coefficient by a unit stone at a non-local scale), and $\sqrt{\kappa}$ is the characteristic width of the mobile convergent front of the low- and high-concentration phases based on the standard solution ($S(\boldsymbol{r}) = \tanh(\frac{r}{\sqrt{2\kappa}})$) of the Cahn-Hillard equation. The term of $\nabla^2 \cdot \kappa\nabla^2 S(\boldsymbol{r})$ behaves like a surface tension term in phase separation, since it protects against over aggregation from the movement caused by lateral squeezing, which would make the stone concentration at location $\boldsymbol{r}$ exceed the maximum allowing value. Such a contribution also arises when the speed of a particle/organism depends on the average concentration in a small local region around the particle/organism on aggregation-behavior systems (34–36).

The theoretical underpinning of phase separation as a form of self-organized pattern formation is derived from the interactions between stones and needle ice, and the resulting velocity-concentration

dependent movement. The movement of stones stems from the growth of needle ice where its height enters into the evolution equation (S3.4) of stones. Here, we describe the height of ice needles with $H(\boldsymbol{r}, t)$ at spatial location $\boldsymbol{r}$ and time t. The dynamics of the height field of ice needles can be expressed as

$$\frac{\partial H}{\partial t} = w_{\text{in}} - aS^m H - rH + D_h \nabla^2 H. \qquad \text{[S3.5]}$$

Here, w_{in} describes the water input in the soil. The second term describes the inhibitory effect of increasing stone cover on needle ice growth; a and m are positive empirical coefficients, and m representing the sensitivity of ice growth inhibit by stone cover. We note that this relationship is nonlinear, as shown in *SI Appendix*, Figure S12, and so take $m = 2$ for quadratic function here. The parameter r is the specific rate of loss of H_2O (both water and ice) due to evaporation, and D_h is the diffusion coefficient describing the H_2O transport process (both for ice and water) during a freeze-thaw cycle. Finally, the time evolution of spatial concentration profiles of mobile stones, and of the height of ice needles, were computed by numerically integrating the two partial differential equations (S3.4) and (S3.5) presented in this study.

The time evolution of the spatial concentration profiles of mobile stones and of the height of ice needles, as given by the two coupled partial differential equations (S3.4) and (S3.5) completely represent our model in its present form, and these are solved below by linear stability analysis and numerically integration.

S3.3. Derivation of effective diffusivity without needle ice interactions. For definiteness, our experimental data has revealed the velocity-concentration relationship in equation (S3.1) which is significant with fitted coefficients on both exponential and hyperbolic functions (*SI Appendix*, Table S2). The Akaike information criterion (AIC) test showed that they are slightly different and even indistinguishable for the fitted curves (*SI Appendix*, Table S2). Note that we used the exponential model because it is the simplest function of convenience in this study.

Based on the experimental relation of $v(S) = v_0 \exp(-\lambda S)$, where v_0 is the speed of an isolated stone, and $\lambda > 0$ controls the decay rate of speed with the increased local concentration. Neglecting the direct influence of the height of ice needles on the stone speed, we have the following first expression on effective diffusivity according to equation (S3.3):

$$D_e(S) = \left[(1 - \lambda S) D(S)\right] \nabla \mathrm{S} = \left[\gamma v_0^2 (1 - \lambda S) e^{-2\lambda S}\right] \nabla S \qquad \text{[S3.6]}$$

with $D(S) = \alpha v(S)^2$. Now, the full dynamics of equation (S3.4) is given by

$$\frac{\partial S}{\partial t} = \nabla \left[(1 - \lambda S) D(S) \nabla S - \kappa \nabla (\nabla^2 S)\right] = \nabla^2 \left[G(S) - \kappa \nabla^2 S\right] \quad \textbf{(Model 1)} \qquad \text{[S3.7]}$$

with $G(S) = (2\lambda S - 1) D(S)/4\lambda$. The function $G(S)$ is called the '*chemical potential*', by analogy with materials science phase separation. Mathematically, the concentration-dependent movement can derive phase separation patterns starting from a uniform distribution when the free-energy function density of equation (S3.7) switches from a single to a double-well shape or from a single valley to a double-valley shape (*SI Appendix*, Figure S13B). Therefore, we can derive the free energy

functional from Eq. (S3.7),

$$\begin{aligned}\mathcal{F}(S) &= \int \left[\int \left\{ G(S) - \kappa \nabla^2 S \right\} \, dS \right] d\boldsymbol{r} \\ &= \int \left[\int \left\{ \frac{(2\lambda S - 1) D(S)}{4\lambda} - \kappa \nabla^2 S \right\} dS \right] d\boldsymbol{r} \\ &= \int \left[\frac{S D(S)}{4\lambda} - \frac{\kappa}{2} |\nabla S|^2 \right] d\boldsymbol{r} + C, \end{aligned} \qquad [S3.8]$$

and $C \in \boldsymbol{R}$ is a constant (essentially irrelevant) new parameter arising from mathematical integration.

We can gain qualitative understanding of the phase-separation conditions that occur in **Model 1** (i.e. Eq. S3.7) via using the free energy functional approach here. In particular, this approach gives a mathematical explanation for the appearance of aggregation stone patterns when exist a condition $D_e(S) < 0$ and for the appearance of dispersion stone patterns when the condition satisfies $D_e(S) > 0$ ((see ref. 34) and *SI Appendix* Figure S13A). For Model 1, the free-energy $\mathcal{F}(S)$ from equation (S3.8) is sketched in *SI Appendix* Figure S13B. There is a single attractive fixed point at the equilibrium $S_{eq} = 1/2\lambda$. Above a higher critical concentration $S_c = 1/\lambda$ the diffusion coefficient in the linear approximation changes sign.

The experimental velocity-concentration relation in equation (S3.1) with phase separation Eq. (S3.7) (named as **Model 1**) indeed leads to spatially self-organized patterns resembling the spatial patterns observed in laboratory experiments (*SI Appendix*, Figure S14 and Fig. 3 in the main text).

S3.4. Effect of the height of needle ice clusters on stones effective diffusivity. Our qualitative experimental evidence shows that a positive interaction exists between the height of ice needle and stones speeds (*SI Appendix*, Figure S2). More generally, this positive relation can be expressed as $v_h(H) = f(H)$ and $\frac{\partial f(H)}{\partial H} > 0$. Here, we look at two scenarios of the specific $v_h(H)$ to elucidate that this phase-separation physical process controls the patterned ground.

For simplicity, we assume that the height of ice needles has a linear positive effect on stone speed, i.e. $v_h(H) = bH$. As a model equation, we assume that this speed follows the simple relationship, $v(S,H) = v_h(H)\, v_s(S)$, i.e. $v(S,H) = \beta H e^{-\lambda S}$ with $\beta = b v_0$. This procedure allows us to analyze the dynamics simple, characterized in the simplest cases by only two dimensionless parameters (β and λ), that may help to explain the origin of self-organized pattern formation across a large class of observed patterned ground in nature and laboratory. This involves a concentration-dependent motility, giving rise to a phase separation that is then arrested at a stable state on a well-defined characteristic length scale by the freeze-thaw cycles. The model presented here is intended to capture only the early stages of the patterning process, and generates patterns that continually coarsen, in contrast to observations. A similar phenomenon occurs in other systems where there are long-range interactions, such as in block copolymers that only exhibit microphase separation at long times. However, at short times, even these systems exhibit phase separations, although the exponent describing the growing length scale is frequently found to be of order 1/4, at least when the interface width is not very small with respect to the domain size (37). It is beyond the scope of the present paper to model the full dynamics of the stone-ice needle interactions.

Now, we have the effective diffusivity derived from equation (S3.3),

$$\begin{aligned} D_e(S,H) &= \left[(1-\lambda S)\gamma\beta^2H^2e^{-2\lambda S}\right]\nabla S + (\gamma\beta^2HSe^{-2\lambda S})\nabla H \\ &= \left[(1-\lambda S)\,D\,(S,H)\right]\nabla S + \left(\gamma\beta^2HSe^{-2\lambda S}\right)\nabla H, \quad \textbf{(Model 2)} \end{aligned} \tag{S3.9}$$

with $D(S,H)=\gamma\beta^2H^2e^{-2\lambda S}$. Hence, the phase separation should be existent in case of scenario 1 with $v_h\,(H)=bH$. This has been confirmed by spatial numerical simulation with the effective diffusivity Eq. (S3.9). The numerical simulation results are shown in *SI Appendix*, Figure S15 with our use of periodic/zero flux boundary conditions.

S3.5. Pattern formation conditions of the phase separation models. Although the theory underlying the variable coefficient partial differential equations is rather complicated, its practical implementation is relatively straightforward with our chemical potential method here. Here, we perform linear stability analysis of Model 1 and Model 2 to obtain the dispersion relation of the patterned-state emergence at early times.

S3.5.1. Linear stability analysis of Model 1. For Model 1,

$$\frac{\partial S}{\partial t} = \nabla^2(G(S)-\kappa\nabla^2S), \tag{S3.10}$$

with $G(S)=\frac{2\lambda SD(S)-D(S)}{4\lambda}$ and $D(S)=\gamma v_0^2e^{-2\lambda S}>0$. Thus the stable points are solutions of $G(S)=0$, i.e. $(2\lambda S-1)D(S)/4\lambda=0$. Since $D(S)>0$, the fixed point is at $S_{eq}=1/2\lambda$, and $G'\,(S)=D(S)(1-\lambda S)>0$, when $S<S_c$. Any spatially uniform concentration field S_0 is a steady state of equation (S3.7), so we linearize about this as an initial condition. Thus, we set $S=S_0+\varphi$ where $S_0>0$ is a constant concentration field that is a steady state solution of equation (S3.7), and obtain the perturbation equation from Taylor series around S_0 and keeping the linear order:

$$\begin{aligned} \frac{\partial\varphi}{\partial t} &= \nabla^2\left[G(S_0)+G'(S_0)\varphi+\mathcal{O}(\varphi^2)-\kappa\nabla^2\varphi\right] \\ &= \nabla^2[D(S_0)(1-\lambda S_0)\varphi-\kappa\nabla^2\varphi]. \end{aligned} \tag{S3.11}$$

Note that in the long wavelength limit, we can neglect $\nabla^2\cdot\nabla^2$ terms here and write equation (S3.11) as

$$\frac{\partial\varphi}{\partial t} = D_{\text{eff}}\nabla^2\varphi \tag{S3.12}$$

with $D_{\text{eff}}=S(S_0)(1-\lambda S_0)$. Note that only for $S_0>1/\lambda\equiv S_0^c$ does negative diffusion to occur (see *SI Appendix* Figure S13), usually a hallmark of spinodal decomposition. Nevertheless, the steady state solution is linearly unstable for a band of wavevectors, as shown by expanding the perturbation φ in Fourier space:

$$\varphi=\varphi_k\sum e^{\sigma(q)t+iq\vec{r}}. \tag{S3.13}$$

Here, $q>0$ is wave number, $i^2=-1$. Substituting equation (S3.13) into equation (S3.12), we obtain the dispersion relation:

$$\sigma\,(q)=D(S_0)(\lambda S_0-1)q^2-\kappa q^4. \tag{S3.14}$$

Linear instability occurs when $\lambda>1/S_0$ and $\Re(\sigma(q))>0$ for pattern formation as was shown in Figure S16.

In summary, model 1 can generate phase separation patterns via a long-wavelength linear instability when $G'(S_0) < 0$, and the $G'(S_0) = 0$ is the critical condition (spinodal instability conditions) for Model 1. The limits of stability from the linear analysis agree with spinodal-decomposition curves through direct numerical simulation, as shown in the main text of Fig. 3A (*Bottom*) in the main text.

S3.5.2. Linear stability analysis of Model 2. Model 2 differs from Model 1 in that it does not possess a family of steady state solutions for any initial stone concentration. Thus, we must expand about the steady state (S_0, H_0) of Model 2, given by should satisfy the following equations

$$\begin{cases} w_{\text{in}} - a{S_0}^2 H_0 - r H_0 = 0 \\ \nabla \cdot D_e(S_0, H_0) = 0. \end{cases} \tag{S3.15}$$

One solution is that $H_0 = \frac{w_{\text{in}}}{aS_0^2 + r}$, $S_0 = \text{const}$, and $D_e\left(S_0, H_0\right) = 0$. Let $S = S_0 + \overline{\delta S}$, and $H = H_0 + \overline{\delta H}$, then model 2 reads

$$\begin{cases} \partial_t(\overline{\delta S}) = \nabla \cdot \phi_1\left(S_0, H_0\right) \nabla^2 \left(\overline{\delta S}\right) \phi_2 + \left(S_0, H_0\right) \nabla^2 \left(\overline{\delta H}\right) - \kappa \nabla^4 \left(\overline{\delta S}\right) \\ \partial_t \left(\overline{\delta H}\right) = -a S_0^2 \ \overline{\delta H} - 2a S_0 H_0 \bar{\delta S} - r \bar{\delta H} + D_h \nabla^2 \left(\overline{\delta H}\right). \end{cases} \tag{S3.16}$$

Here, $\phi_1\left(S, H\right) = \gamma\beta^2 H^2(1 - \lambda S)e^{-2\lambda S}$, and $\phi_2\left(S, H\right) = \gamma\beta^2 H S e^{-2\lambda S}$. Now we expand the equations (S3.16) in Fourier space, i.e.

$$\begin{pmatrix} \widehat{\delta S} \\ \widehat{\delta H} \end{pmatrix} \propto e^{iqx + \sigma(q)t}.$$

The equations (S3.16) read now as

$$\sigma \begin{pmatrix} \widehat{\delta S} \\ \widehat{\delta H} \end{pmatrix} = \overbrace{\begin{pmatrix} -\phi_1\left(S_0, H_0\right) q^2 - \kappa q^4 & -\phi_2(S_0, H_0) q^2 \\ -2a S_0 H_0 & -a S_0^2 - r - D_h q^2 \end{pmatrix}}^{=\mathcal{M}} \begin{pmatrix} \widehat{\delta S} \\ \widehat{\delta H} \end{pmatrix} \equiv \mathcal{M} \begin{pmatrix} \widehat{\delta S} \\ \widehat{\delta H} \end{pmatrix}. \tag{S3.17}$$

Then we obtain the eigenvalues of Model 2 with the matrix of $\mathcal{M}$ from the above equation (S3.17). The linear instability is obtained when $\Re(\sigma(k))$ of matrix $\mathcal{M}$ is positive. For long-wavelength instability, we can numerically calculate the intervals of the positive values of $\Re(\sigma(q))$ on the (S_0, λ)-space was shown in *SI Appendix*Figure S17 and Fig. 3B (*Bottom*) in the main text. Both the numerical simulations and linear stability analysis qualitatively predict a coincident region where the phase separation patterns appear. One may see the deviation of the right-boundary spinodal curve caused by the limitation of the time scale for our numerical simulation.

Note that Model 2 does not possess a '*chemical potential*' like Model 1, so is not manifestly of the phase separation type. In future work, a more refined analysis of the coupling between ice crystals and stone concentration will be provided. Nevertheless, Model 2 demonstrates a point of principle that there can be pattern-forming instabilities in the coupled stone-ice needle system.

S3.6. Modelling phase separation – a summary. Spatial self-organization theory often predicts the macroscopic scale behavior resulting from system-specific microscopic rules and interactions. Commonly, the system behaviors at coarse-grained level are difficult intuitively to obtain from these simple rules at individual levels, named as emergent properties. Here, we follow such an approach in

previous study (34, 38), offering a description on scales intermediate between microscopic dynamics of stones and the macroscopic scale of the self-organized patterned ground in the laboratory and field. Unlike the widely studied Turing mechanisms (39, 40) for self-organized patterning, we proposed the phase separation process, based on local concentration-dependent feedback, whereas the self-organized Turing patterns are stationary for spatial pattern scales and non-conservation on particles. The models will help us to identify a very general mechanism that explains the origin of pattern formation across a large class of experiments and field observations in nature.

As described in Figure 3 in the main text, our models reproduce patterns similar to the observed in self-organized stone patterns observed in our experiments. However, there are some unresolved issues. Model 1, which ignores the ice needle-stone feedback, predicts that the pattern formation process resembles phase separation in materials science, with the governing equation being of the form of the Cahn-Hilliard equation. Indeed simulations show the same early time coarsening behavior as experiments (Figure 5 in the main text), including data collapse and the tail of the structure functions. The way in which the characteristic length scale grows with time is empirically dependent on whether the ground is level or sloping, but the model is not capable of making this distinction. It is possible that the scaling exponents reflect the interface structure, as is known to occur in other systems where there is a saturation in the growth process, such as block copolymers (37). Thus, the process by which the pattern scale saturates at long times is not captured by our current models.

One of our key findings is that ultimate patterns produced by the phase separation process depend on the initial stone concentration. The stone island, labyrinthine, and circle patterns can generate from lower stone concentration to higher stone concentration in spinodal phase separation. This phase diagram structure also agrees with the laboratory evidence from low to high stone concentration (Figure 3 B–D in the main text).

The basic phase separation mechanism is not limited to the present example. In our experimental system, the phase separation process induced by differential needle ice height between high and low stone concentration regions, results in stone separation and accumulation, self-forming islands, labyrinths, circles on level ground and stripes on sloping ground. However, needle ice activity is a special case which produces small-scale patterned ground and most large-scale patterned ground formation is induced by differential frost heave of ground ice or segregated ice in the active layer (28, 29). In such a case, our robust model can also provide a potential explanation of large-scale patterned ground by building a relationship between stone concentration with frost heave induced by segregated ice. Phase separation as a pattern forming mechanism has been successful in biology and ecology (38, 41, 42), and we hope that our experimental and theoretical framework here extends this understanding to the realm of geomorphology realm to the phase separation principle in the future.

S4. Robustness of the different stone speed forms

Our experimental data suggest that other speed functions may also be a reasonable choice as listed in Table S2. Specifically, the exponential and quadratic functions are almost indistinguishable when fitting the relation between local coverage and movement speed. For the sake of simplicity, and without loss of generality, we have chosen an exponential relation for both models. A parallel analysis was implemented following the present framework for different specific formulas. This showed that similar phase separation patterns are produced when we replace the exponential function with a quadratic function as suggested, in Table S2. In this appendix, in Figure S18,

we show an example of self-organized patterns resulting from the proposed phase separation model 1 and with the quadratic function of Table S2. We have deposited the codes in GitHub (https://github.com/liuqx315/Phase-separation-patterned-ground) for the reader to further explore. Here, the phase separation model with a two-scale feedback leads to the stationary Turing-like patterns, as was shown in a previous study on mussel beds ecosystems (31). In contrast, our data suggest rejecting that the hypothesis of a two-scale feedback can be rejected (see Figure S6).

S5. Supporting Information Tables

Table S1. List and description of all the experiments conducted in the Earth Surface Processes Laboratory (University of Tsukuba, Japan).

	Run	SZ (mm)	Cover/NS	RT (h)	Slope (°)	HIN Minimum	HIN Maximum
Level ground	1	4 – 8	20%(648)	360	0	14.5 ± 0.1	40.0 ± 0.1
	2	4 – 8	30%(912)	360	0	16.7 ± 0.1	39.0 ± 0.1
	3	4 – 8	40%(1226)	360	0	26.9 ± 0.1	41.5 ± 0.1
	4	4 – 8	60%(1916)	360	0	14.7 ± 0.1	44.3 ± 0.1
	5	4 – 8	80%(2597)	360	0	19.4 ± 0.1	46.6 ± 0.1
Sloping ground	6	4 – 8	20%(684)	240	5	11.8 ± 0.1	24.7 ± 0.1
	7	4 – 8	20%(684)	360	7	16.7 ± 0.1	25.4 ± 0.1
	8	4 – 8	20%(684)	240	9	13.7 ± 0.1	32.2 ± 0.1
	9	4 – 8	20%(684)	240	11	13.8 ± 0.1	25.0 ± 0.1
	10	8 – 16	20%(586)	240	7	11.5 ± 0.1	25.1 ± 0.1

Note: SZ=Stone Size, NS=Numbers of Stone, RT=Run Time, HIN=Height of ice needles.

Table S2. Model selection of the experimental relationships between stone speed and local stone concentration

Mathematical formula	AIC	Parameters	p-value	N
Formula 1: Exponential function $v(\rho) = v_0 \exp(-\lambda\rho)$	7243.1	$v_0 = 2.02, \lambda = 0.85$	0.0001	1584
Formula 2: Quadratic function $v(\rho) = p_0 - p_1\rho + p_2\rho^2$	7242.6	$p_0 = 2.09, p_1 = 2.47$ $p_2 = 1.73$	0.0001	1584
Formula 3: Two scale-feedbackfunction $v(\rho) = 1/[p_0 + p_1 C_S(\rho) - p_2 C_L(\rho)]$	-3164.1	$p_0 = 0.55, p_1 = 0.61$ $p_2 = 0.46$	0.01	1584

Note: $C_S(\rho)$ and $C_L(\rho)$ represent the stone concentration of the movement stone at the small and large scale, respectively.

Table S3. Definitions and interpretation of variables and parameters in phase separation models

Symbol	Value	Unit	Definition and Interpretation
v_0	2.02	mm/h	Maximum stone speed of an isolated stone
λ	3.0*	–	Decay rate of stone speed with increased neighbor concentration
κ	0.15	–	Tension coefficient of gradient energy controls the length of transition regions between two phases
w_{in}	$0.1 \sim 0.5$	g/h	Input of the water
a	0.2	g/h	Inhibited coefficient by stone concentration
D_{h}	5	cm^2/h	Diffusion coefficient describing the H_2O (both water and ice) transport process during a freeze-thaw cycle
β	0.2	–	Positive feedback coefficient of needle ice on stone speed
r	0.01	$1/h$	Specific rate of loss of the H_2O (both water and ice) due to evaporation during a freeze-thaw cycle

*A similar sorted patterned ground also gets at 0.85 of experimental data, but for different ranges for stone concentrations (see Figure 3 in the main text for details). See the online codes for the different phase separation patterns with the various parameter values listed here.

Table S4. **Potential processes and field evidence on the diversity of patterned ground in nature.**

Form	Processes assumed to be responsible	Based on	Location (country)	Reference
Circles, stripes	Needle ice growth, ice lens, Wind action, convection cells	Field observation	Marion Island	(5, 6)
Circles	/	Field observation	Barton Peninsula, King George Island, Antarctica (62°S)	(7)
Circles	Rapid frost-sorting	Field observation	Jotunheimen, Norway	(8)
Circles	Frost plug, Coalescence of plugs	Field observation	Devon Island, Nunavut, Canada	(9)
Circles	circulation mechanisms	Field observation	Northern Billefjorden area, central Svalbard	(3)
Circles	Soil-circulation	Field obeservation	Resolute area, Cornwallis Island, Canadian High Arctic	(10)
Circles	Differential frost heave	Field observation	Central Alaska	(11)
Circles, stripes, labyrinths	Sorting by deep seasonal freezing	Field observation	Lesotho-South Africa	(12)
Circles, labyrinths	Differential frost heave, Lateral sorting, squeezing, convective soil movements	Field observation, Numerical simulation	Kvadehuksletta, western Spitsbergen	(29, 43)
Polygons, nets	Differential frost-heave action, frost cracking	Field observation.	Krkonoše Mountains, Czech Republic	(13, 14)

Table S4. **(continued)**

Form	Processes assumed to be responsible	Based on	Location (country)	Reference
Polygons, stripes	Frost-jacking, differential frost heave	Field observation	La Mortice, French Alps	(2)
Stripes	/	Field observation	Jotunheimen, Norway	(15)
Stripes	Mechanical weathering, frost shattering Differential frost heave	Field observation	Ledenica pod Hrusivo ice cave, western Slovenia	(16)
Stripes	Needle-ice growth	Field observation, Numerical simulation	Mauna Kea, Hawaii, USA	(44)
Stripes	Frost heaving, sorting, dynamics of the flux of coarse sediment	Field observation	Cordillera Real, 16°S (Bolivia)	(17)
Stripes	Differential frost heave	Field observation	Lake District. Northern England	(18, 19)
Stripes	Differential frost heave	Field observation and lab experiment	Upper Engadin, Swiss Alps	(20)
Stripes, nets	Differential frost heave	Field observation and Laboratory	Colorado alpine region	(21)
Nets	needle-ice growth and frost heave	Field observation	Fláajökull (Southeast Iceland) and Elisbreen (Northwest Spitsbergen)	(22)

S6. Supporting Information Figures

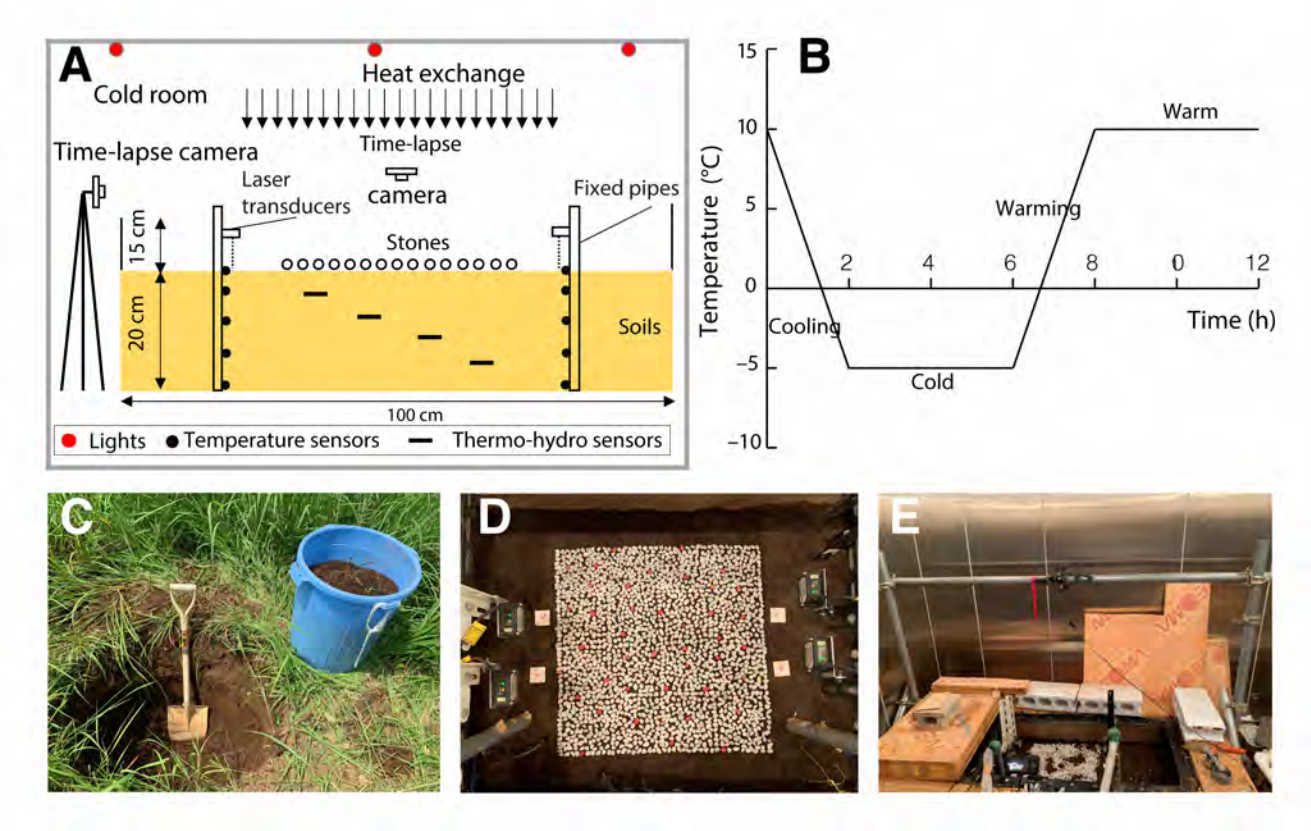

Fig. S1. Experimental set-up. (A) Schematic of experimental set-up. (B) Controlling temperature in room during one freeze-thaw cycle. (C) Soil samples used in our experiment from field site in University of Tsukuba, Japan. (D) and (E) Top and side view of experimental arena.

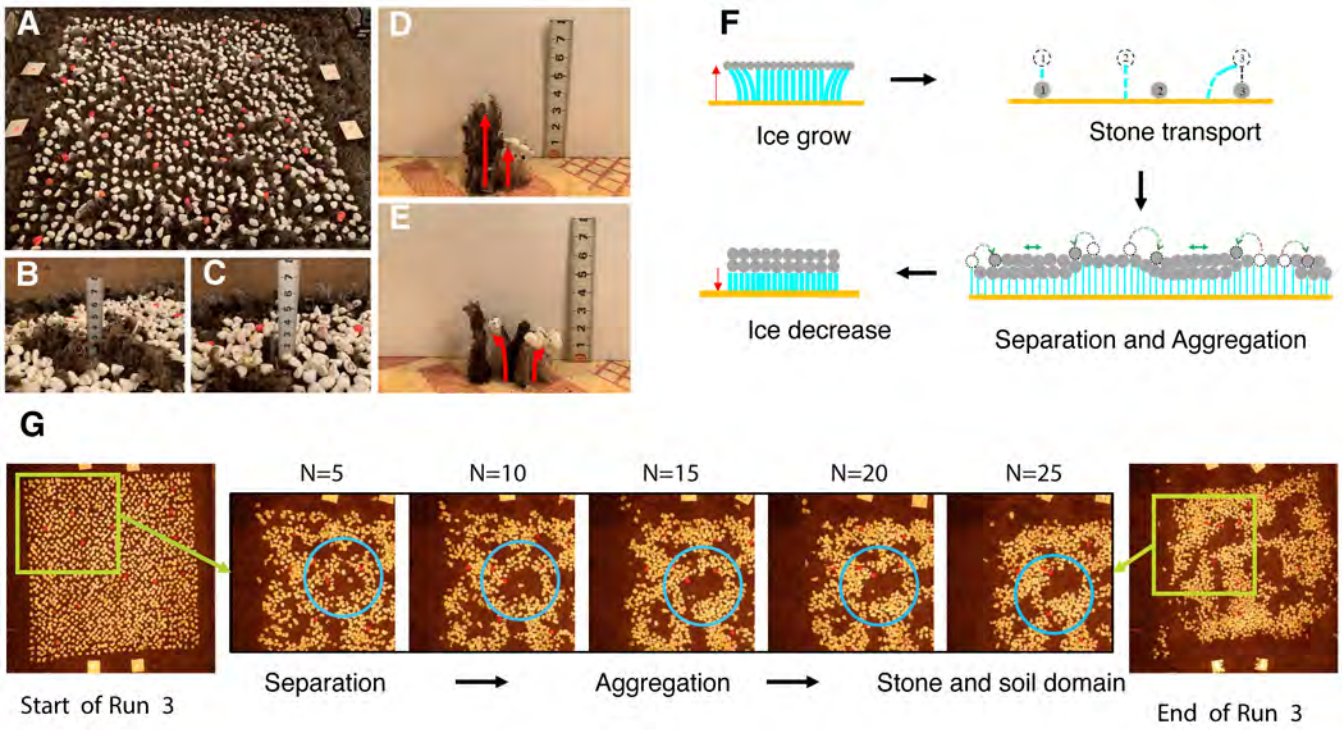

Fig. S2. Experimental measurements of relationship between needle ice activity and stone transportation. (A) A snapshot of needle ice activity at $t = 6.5$ h with 30% stone cover in the first freeze-thaw cycle. (B) and (C) Needle ice growth within soil domain (~ 4 mm) (B) and stone domain (~ 2 mm) (C) at $t = 366.5$ h (31st freeze-thaw cycle) with 40% stone cover. (D) and (E) Observed/measurement straight needle ice height (D) and curved needle ice (E) at $t = 366.5$ h (31st freeze-thaw cycle) with 40% stone cover. (F) Schematic diagram of stone transport by needle ice and negative feedback between stone concentration and needle ice height (Movie S4). (G) Stone separation and aggregation by needle ice during freeze-thaw cycles. N represent the number of the freeze-thaw cycles.

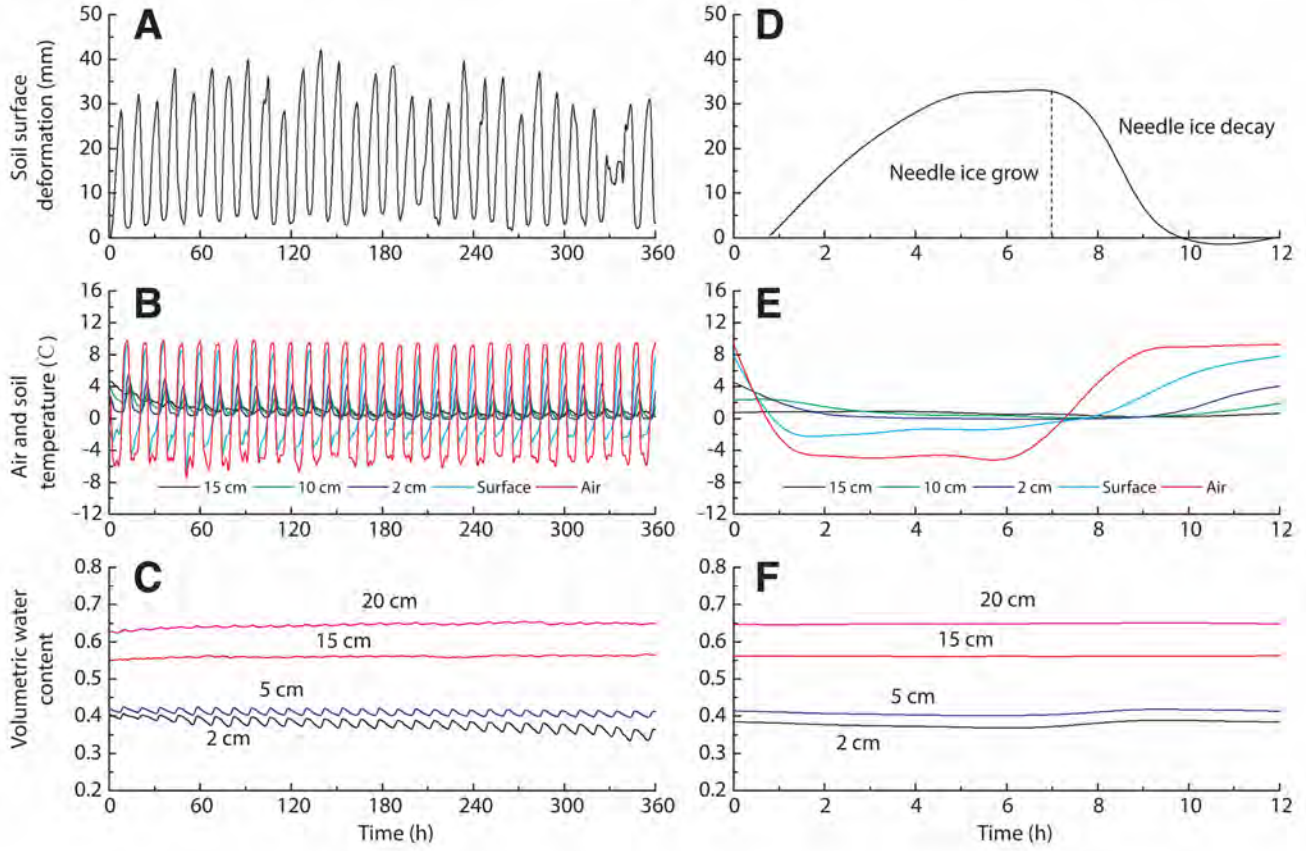

Fig. S3. Soil surface deformation, air and soil temperature, volumetric water content conditions during whole experimental period and 16th cycle in experiment with 40% **stone cover**. (A to C) Soil surface deformation (A), air and soil temperature (B) and volumetric water condition (C) in experiment with 40% stone cover during 30 freeze-thaw cycles recorded with two data logging systems. (D to F) Soil surface deformation (D), air and soil temperature (E) and volumetric water condition (F) in experiment with 40% stone cover during 16th freeze-thaw cycle.

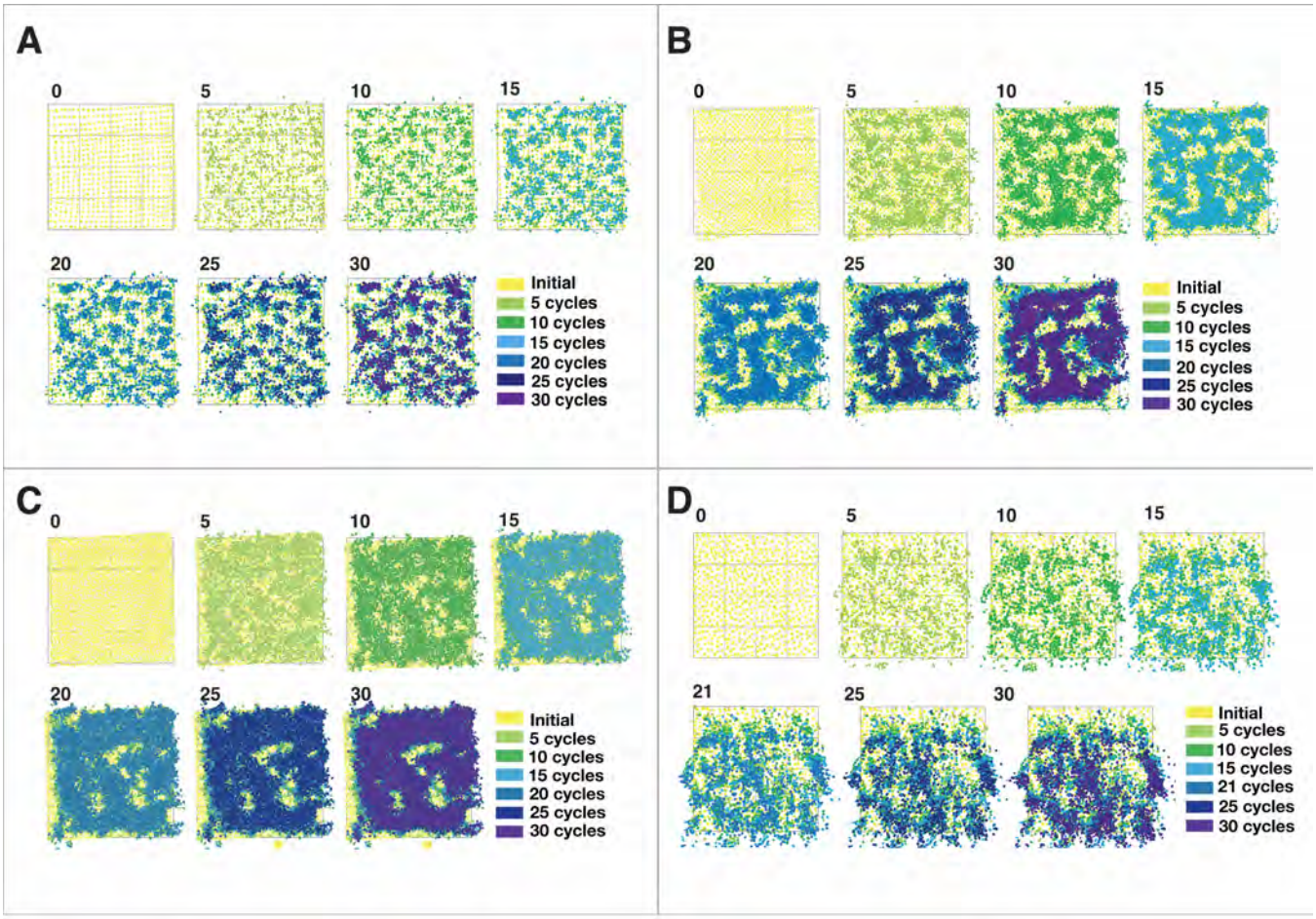

Fig. S4. Patterned ground evolution in the experiments. Tracking all surface stone locations at five freeze-thaw cycle intervals. (A to C) Diverse patterns resembling stone-free islands (A), stone polygons (B), and circles (C) with 20%, 40%, and 60% stone cover on level ground, respectively. (D) Elongated, stripes-like patterns with 20% stone cover on 7° sloping ground (ref. 24).

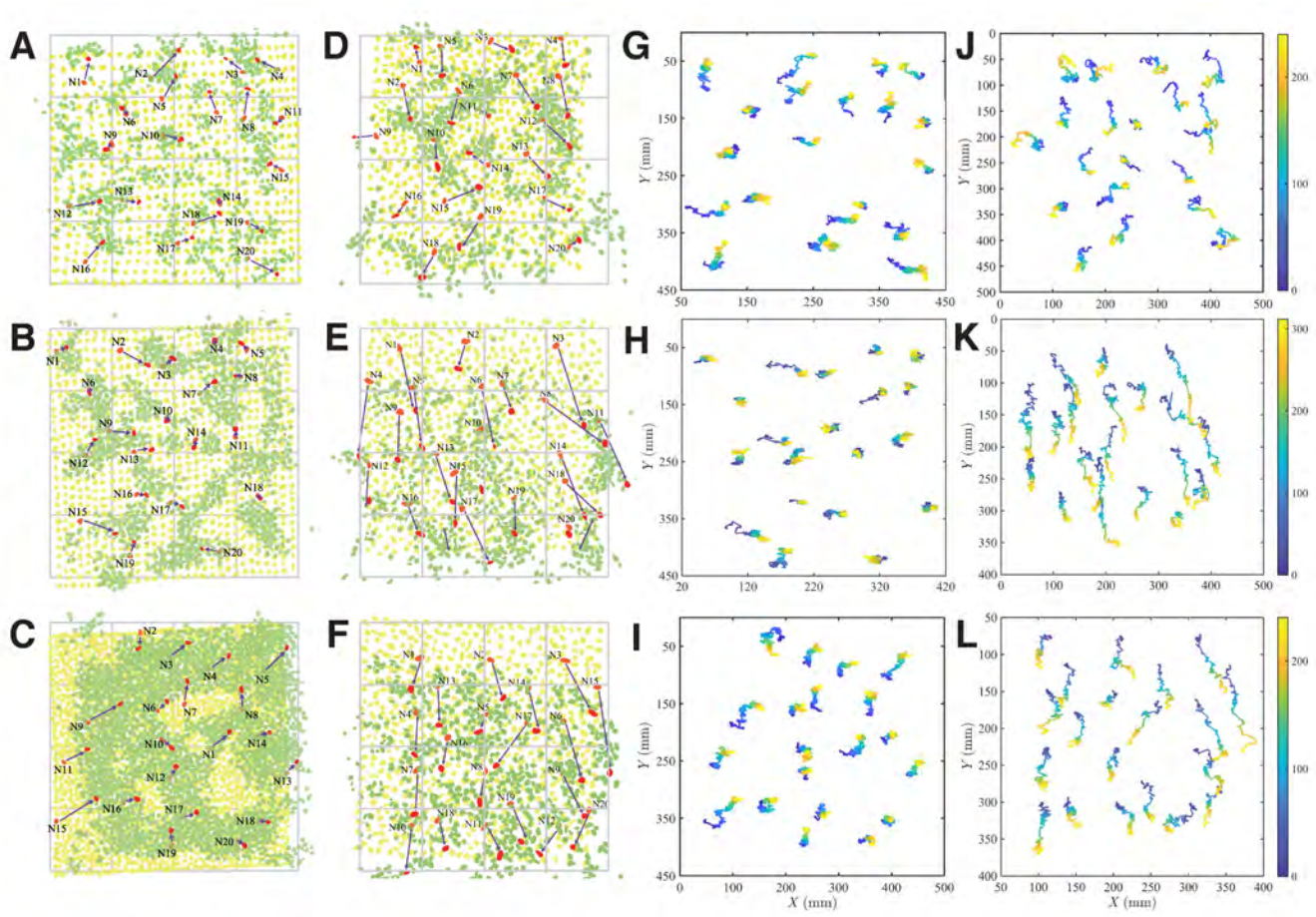

Fig. S5. Stone motion in the experiments. (A to F) Initial and final stone positions in experiments with 20% (A), 30% (B) and 60% (C) stone cover on level ground and 20% stone cover on a ground surface inclined 5° (D), 7° (E) and 9° (F) (ref. 24). Red dots represent 20 stones selected for trajectory tracking. Yellow and green colors indicate initial and final stone positions. (G to L) stone trajectories corresponding to (A to F) panels respectively, illustrating characteristic movement toward stone aggregations and clusters, as well as downslope. Color bars represent the time (hours) progression in lab experiments.

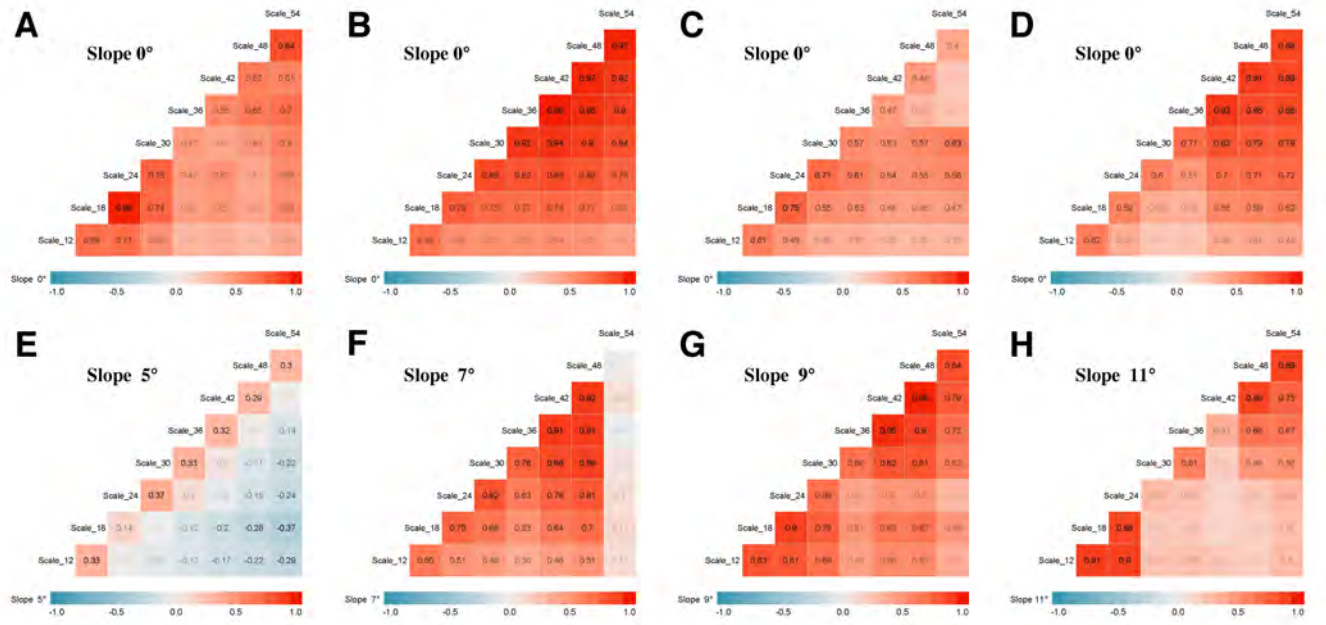

Fig. S6. The coefficient of movement speed with increased spatial scales from 12 mm to 54 mm in the experiments. (A to D) Multi-scale matrix of correlation coefficient of increased spatial scales from 12 mm to 54 mm in experiments of 20% (A), 30% (B), 40% (C) and 60% (D) stone cover on level ground. (E to H) Multi-scale matrix of correlation coefficient of spatial scales increased spatial scales from 12 mm to 54 mm in experiments of 20% stone cover on sloping ground with 5° (E), 7° (F), 9° (G), 11° (H) slope gradient. The results come from general linear model with R package (45, 46).

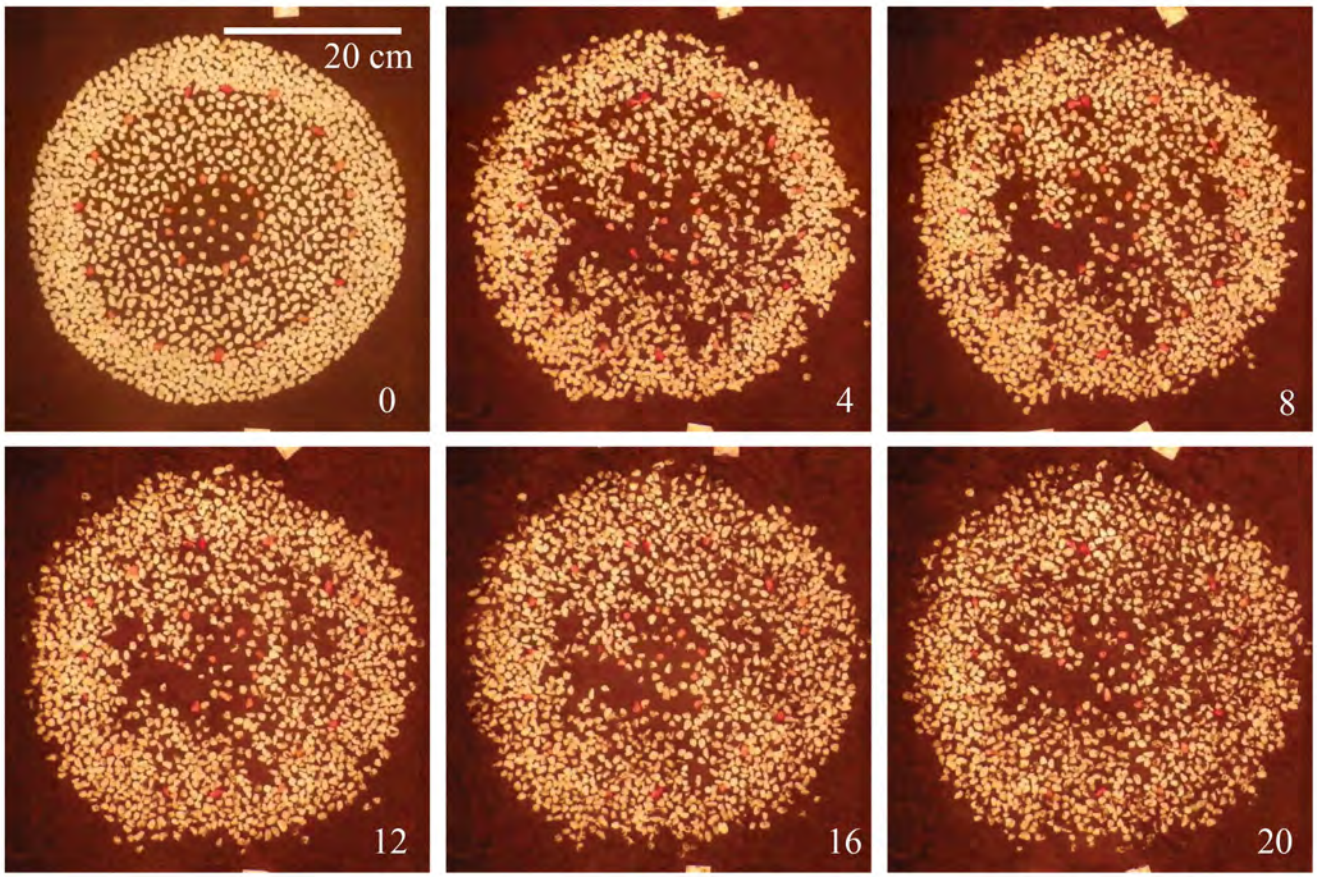

Fig. S7. Spatial pattern development starting from a uniform triple concentration (80%, 40%, 10% from edge to inward direction) through 20 freeze-thaw cycles. The numbers within each panel depict the i^{th} freeze-thaw cycles.

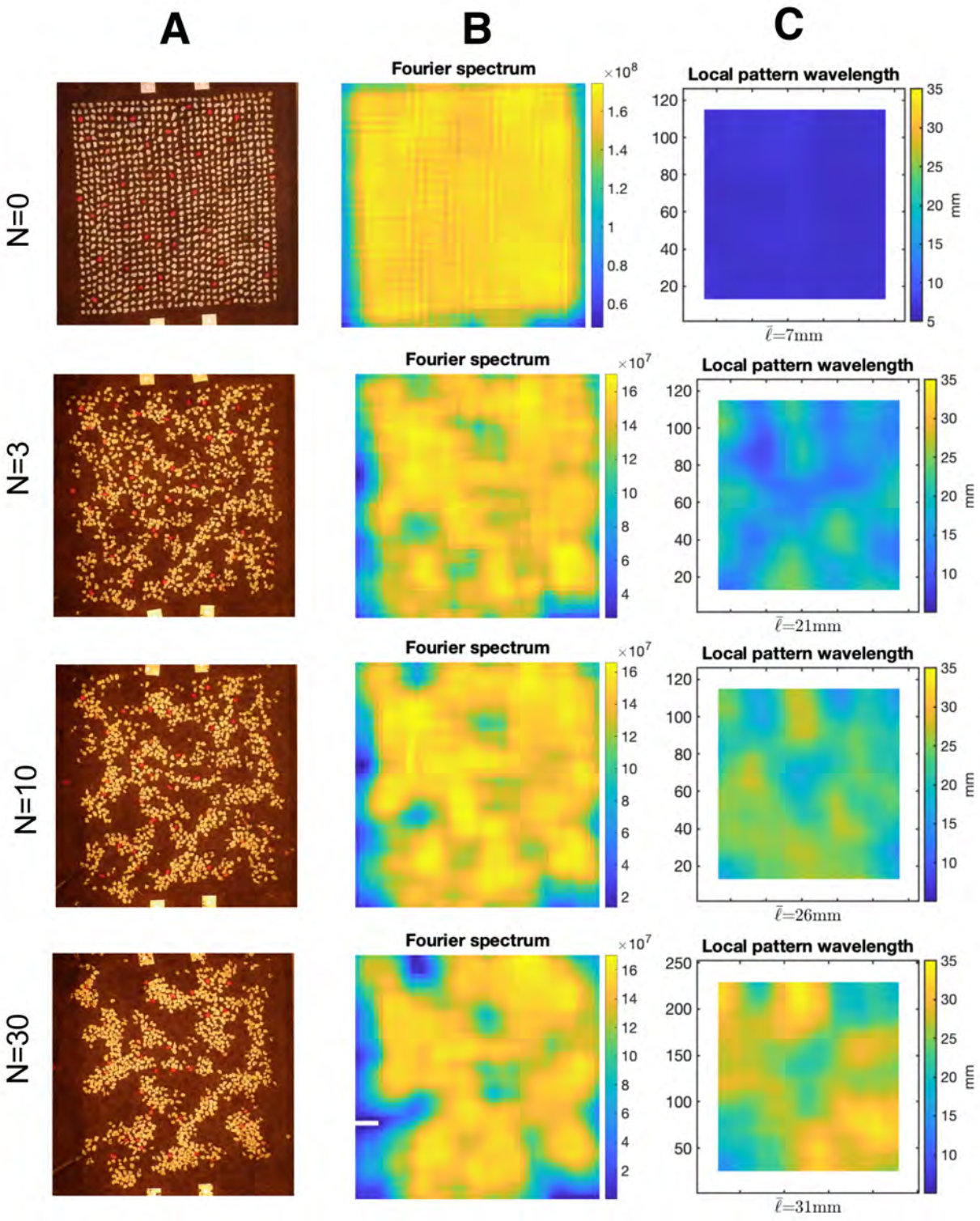

Fig. S8. 2D Fourier transforms in image processing. (A) Initial image and images of stone patterns in experiment with 30% stone cover after 3, 10, 30 freeze thaw cycles from top to bottom rows (N represent numbers of freeze-thaw cycles). (B) and (C) Fourier spectrum (B) and local pattern wavelength (C) corresponding to column of panel (A), respectively. The global mean wavelength $\bar{\ell}$ was calculated by average of peak values of the local pattern wavelengths in rows and columns.

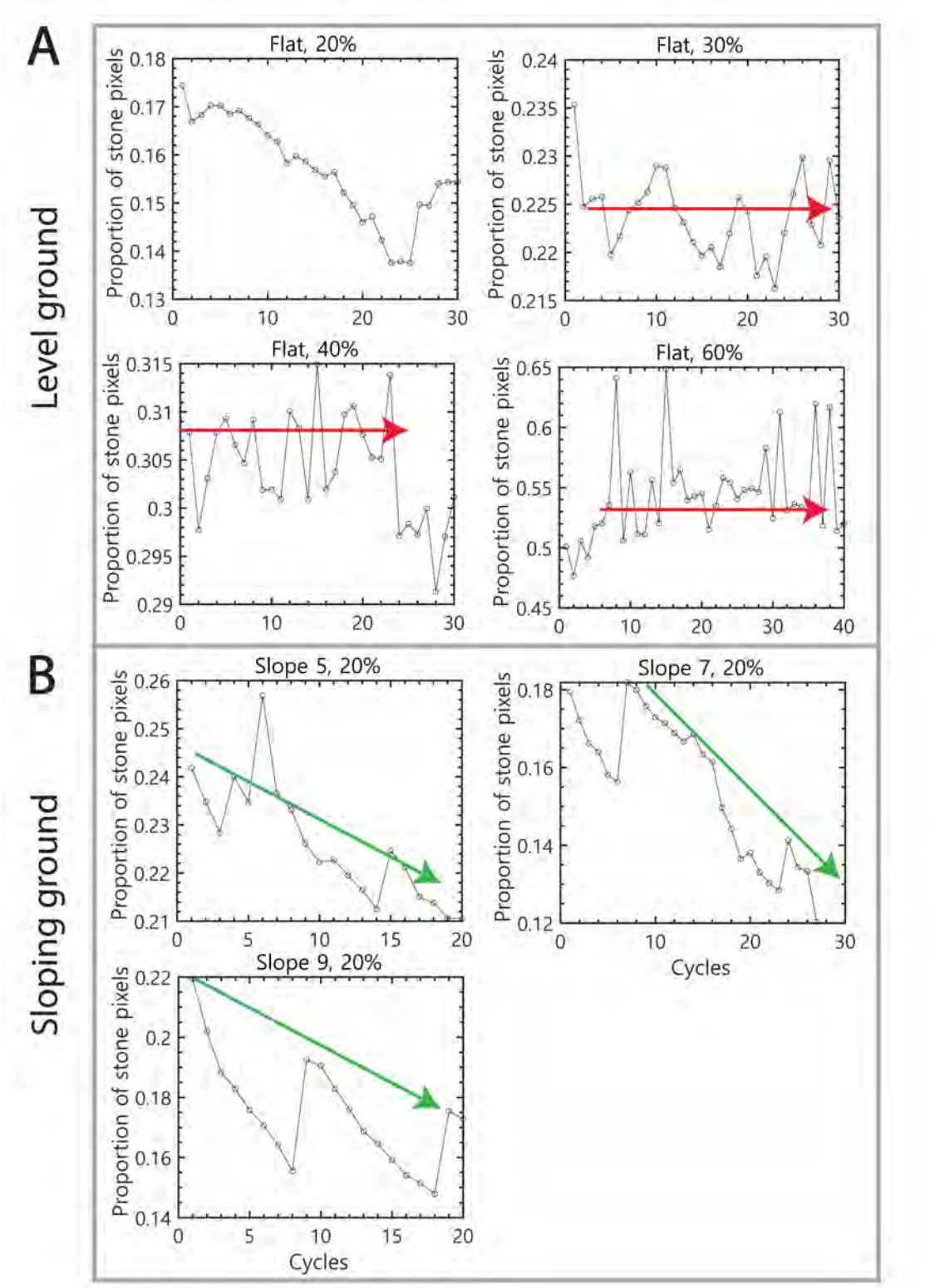

Fig. S9. Overlapping of stones with freeze-thaw cycles. (A) Changes of four coverage rates on the level ground scenario. Note that at the 20% case, the declined coverage rate doesn't attribute to overlapping, but stones mixed with soil color. (B) Changes of three coverage rates on the sloping ground cases.

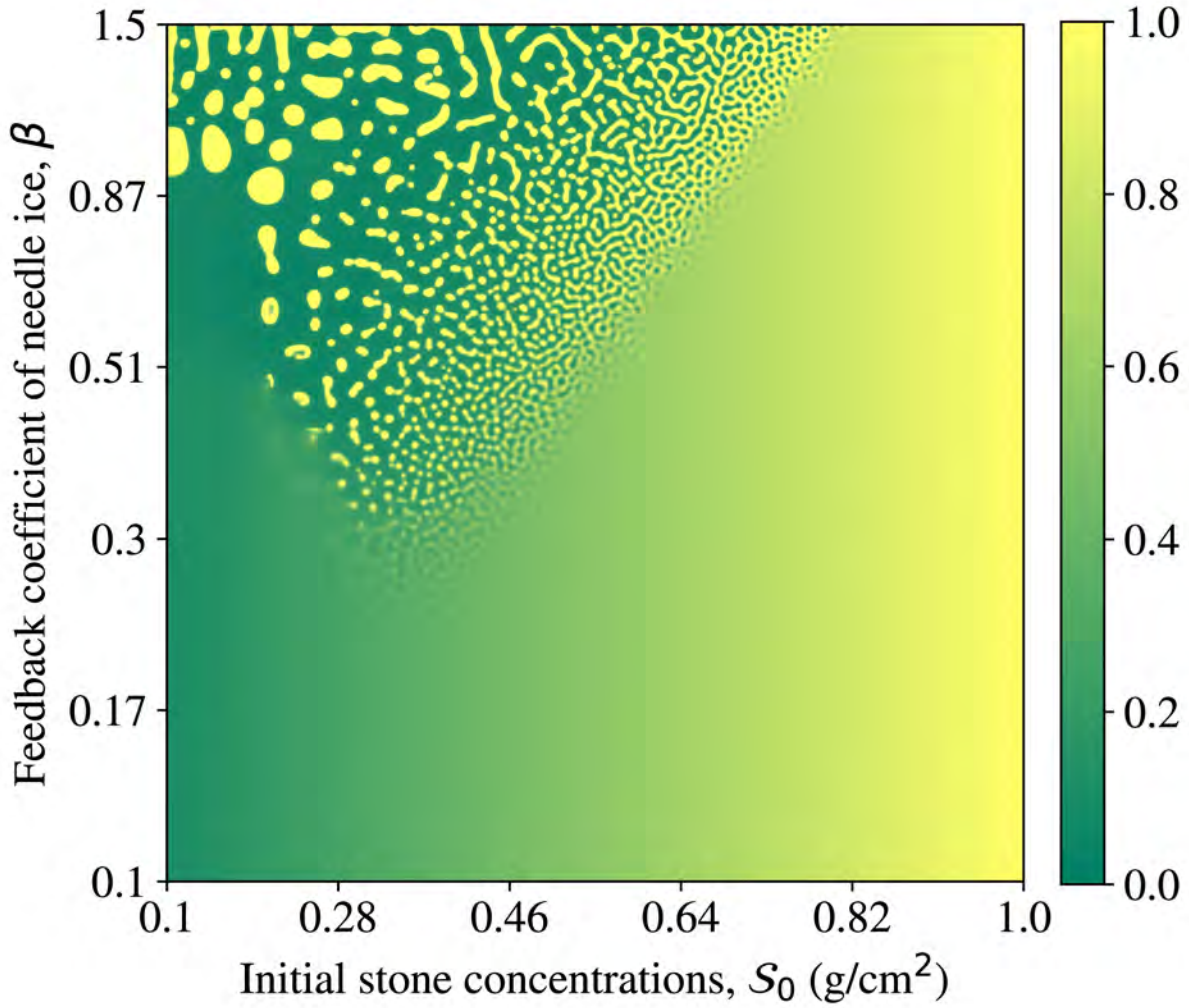

Fig. S10. Feedback effect of needle ice on the sorting pattern formation. The phase diagram for the model 2 depicts patterns formation with stone concentration and feedback strength (β) determining the regions in which the phase separation switches from the one-phase to two-phase regimes along environmental gradient. The system does not undergo phase separation below the critical strength (β_c) for the high stone concentration. The simulation was obtained from the parameters that were shown in Fig. 3B in main text but $\lambda = 3.0$, and $w_{\text{in}} = 0.2$.

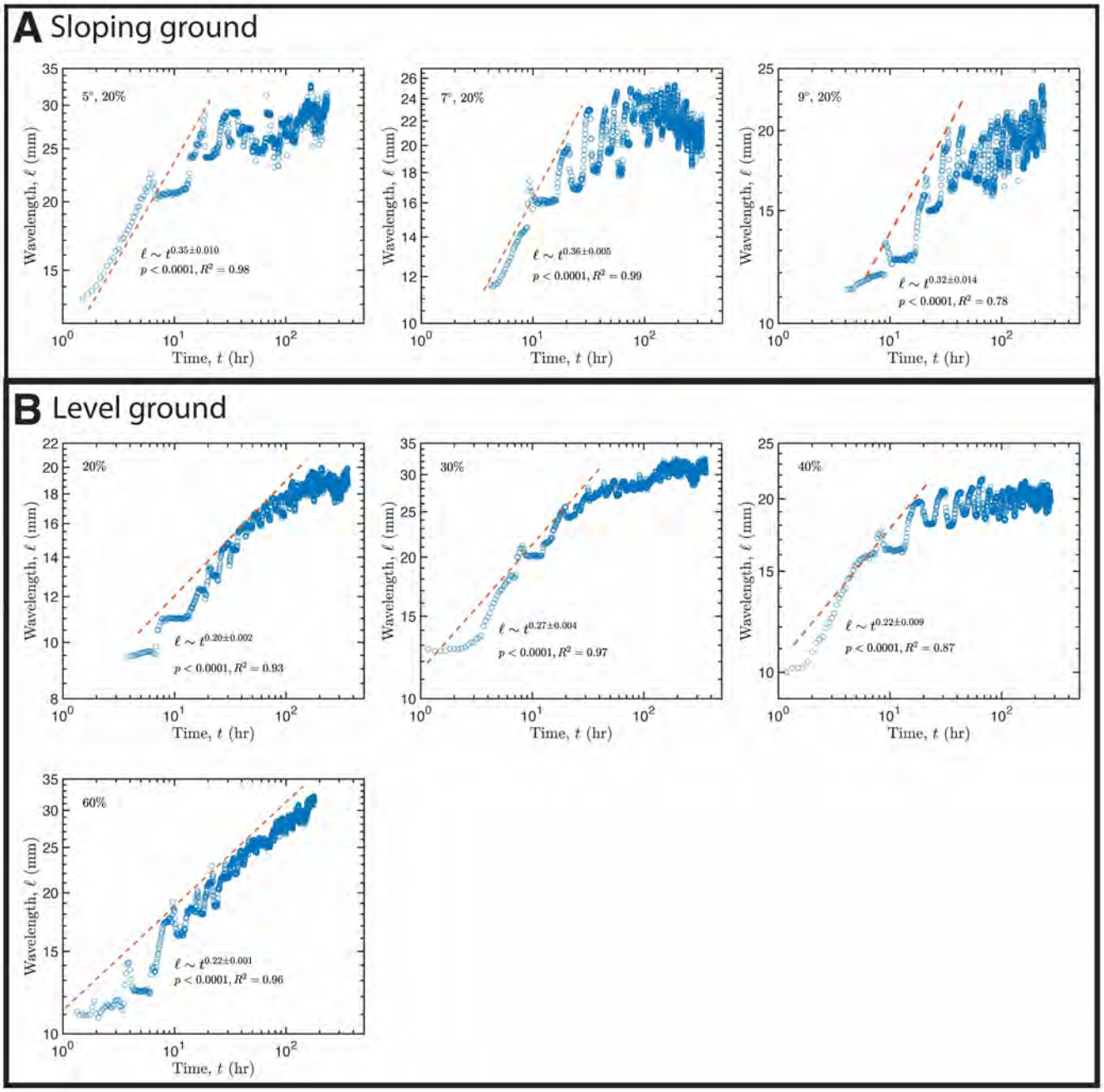

Fig. S11. Scaling behavior of coarsening patterns of each experimental evolution on the sloping ground (A) and level ground (B), respectively. They display a similar power-law exponent associated with a slight deviation. See Table 1 for the detailed statistical properties.

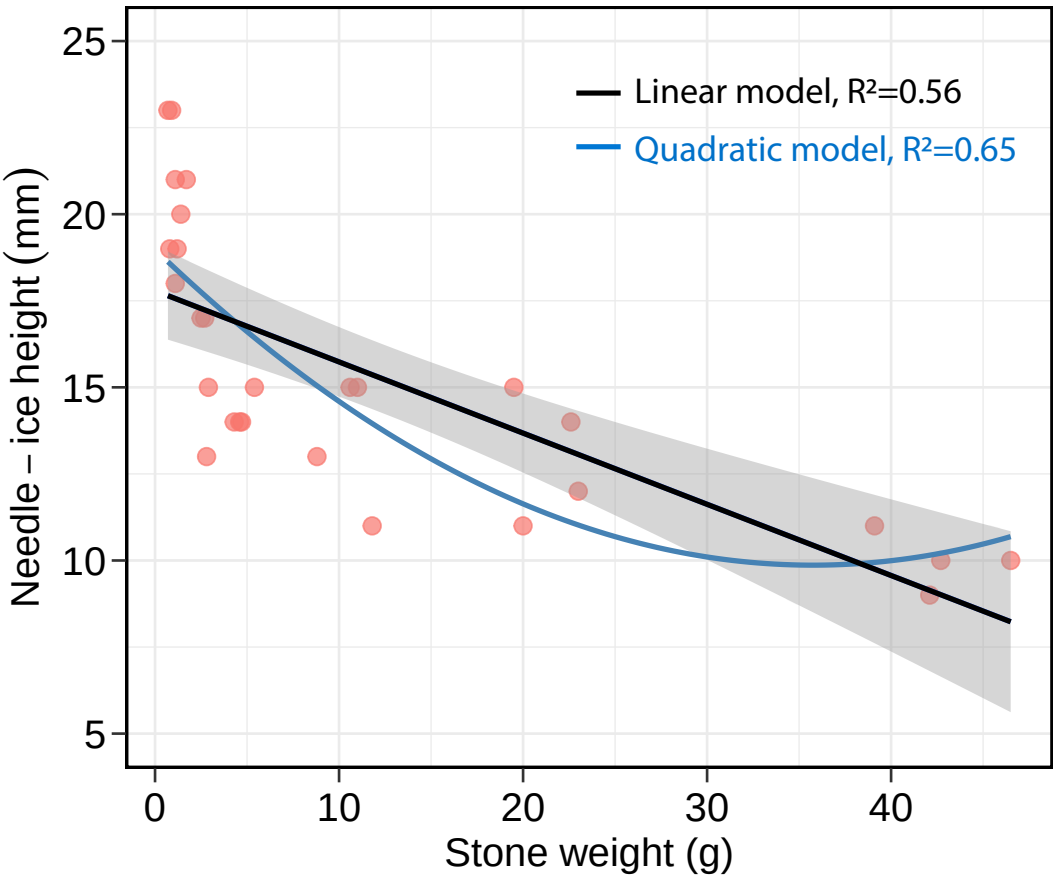

Fig. S12. Inverse nonlinear relationship between needle ice height and stone weight. The lines are trends, and shaded area indicate the 95% CI of the fixed effect.

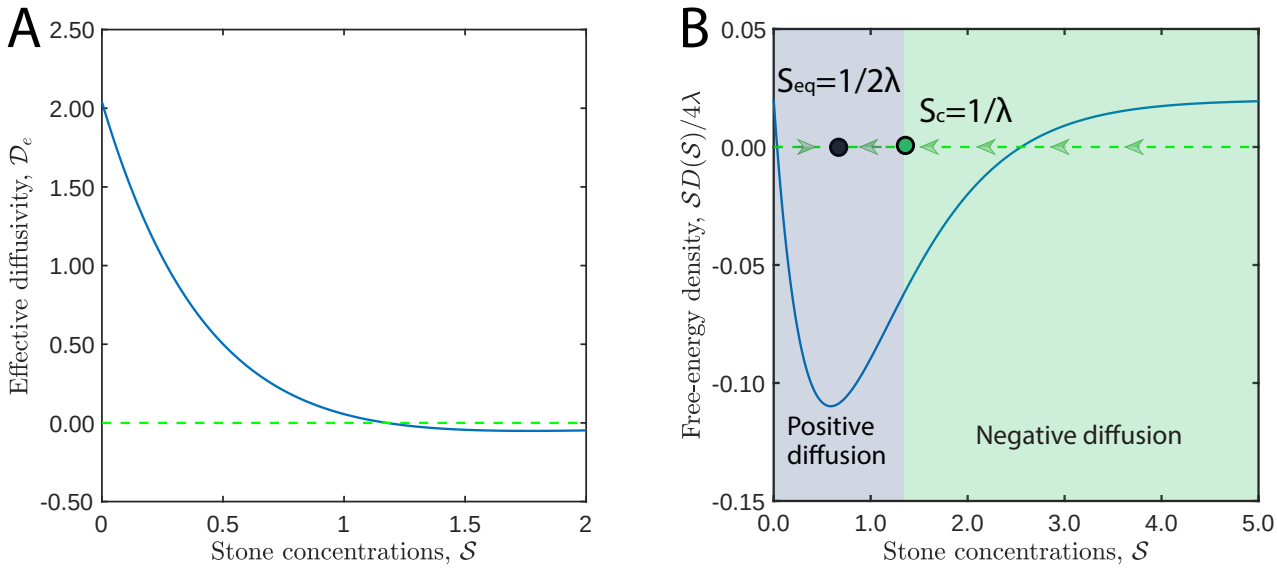

Fig. S13. Two analytical plots of effective diffusivity $D_e(S)$ (A) and free-energy density of $\mathcal{F}(S)$ (B) on our Model 1 (i.e. Eq. (S3.8)) with the experimental relationship of $v(S) = v_0 e^{-\lambda S}$ with parameters $\lambda = 0.85$, $d = 2$, $\tau = 1.0$, and $v_0 = 2.02$. Dashed lines describe zeros as a reference for comparison for reasonable input status. The dots represent two statuses of low (or high) concentration driven by the phase separation processes.

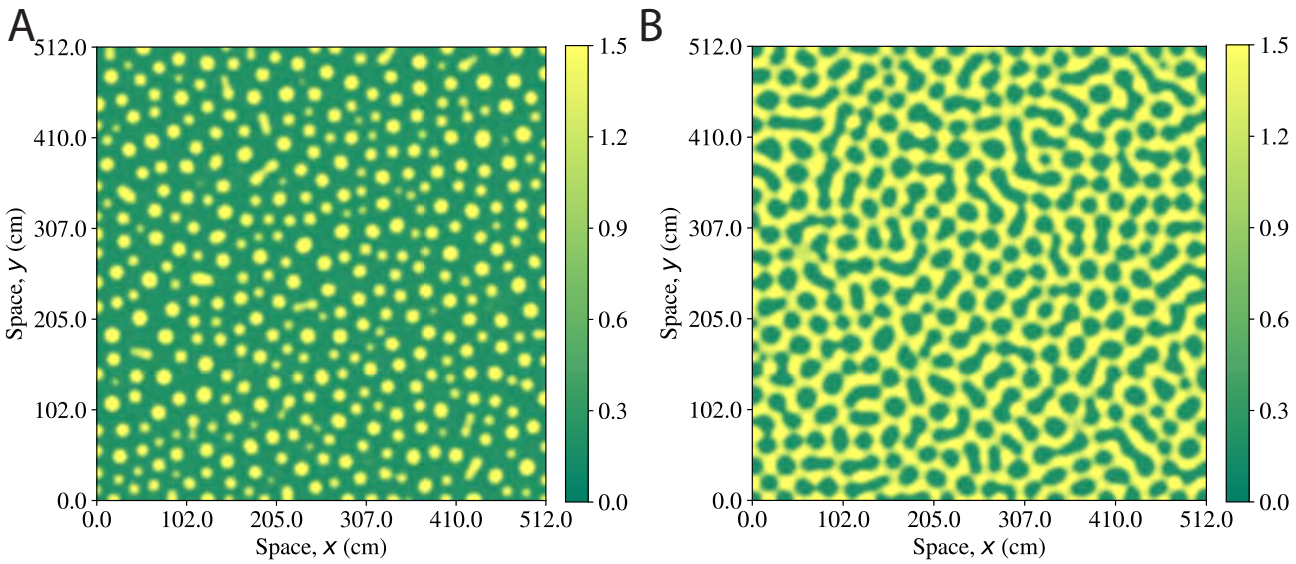

Fig. S14. Two snapshots of simulation results on model 1 with $v(S) = v_0 e^{-\lambda S}$ for different initial stone concentration at 0.5 (A) and 0.85 (B) respectively at $t = 5000$. The numerical simulations were implemented on periodic boundary conditions with parameters $\lambda = 3.0$, $d = 2$, $\tau = 1.0$, and $v_0 = 2.02$. Colorbars represent the stone concentrations with unit g/cm^2.

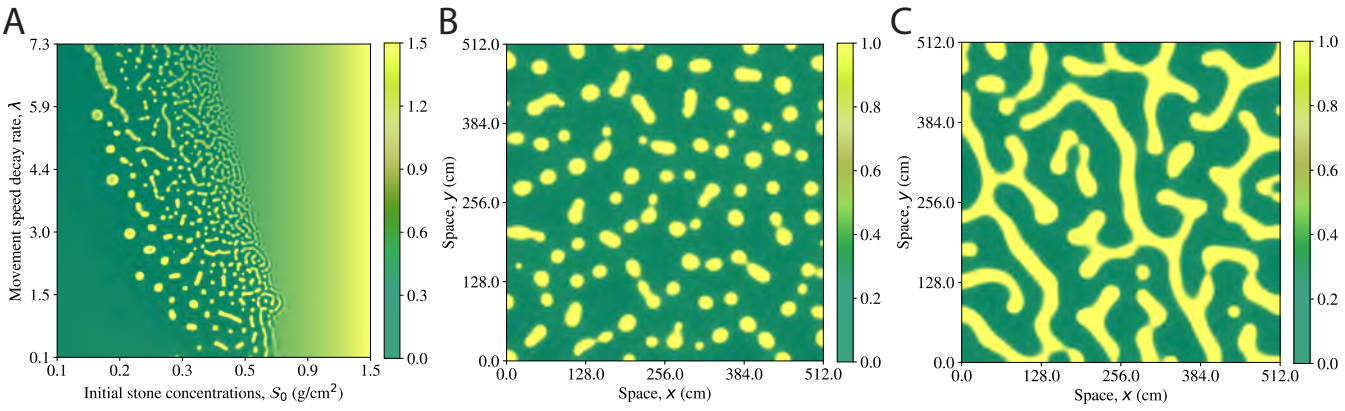

Fig. S15. (A) phase diagram on the (S_0, λ) plane for pattern formation based on Model 2 with the effective diffusivity Eq. (S3.9). (B, C) Two typical patterns of the numerical simulation for various stone concentrations with parameters $\lambda = 3.0$, $S_0 = 0.2$ (B) and $\lambda = 3.0$, $S_0 = 0.4$ (C). The other parameters are listed as *SI Appendix*, Table S3. Colorbars represent stone concentrations with unit g/cm^2 for panels. Note that the right-boundary spinodal line of the panel (A) depends on the time scales of the model simulation.

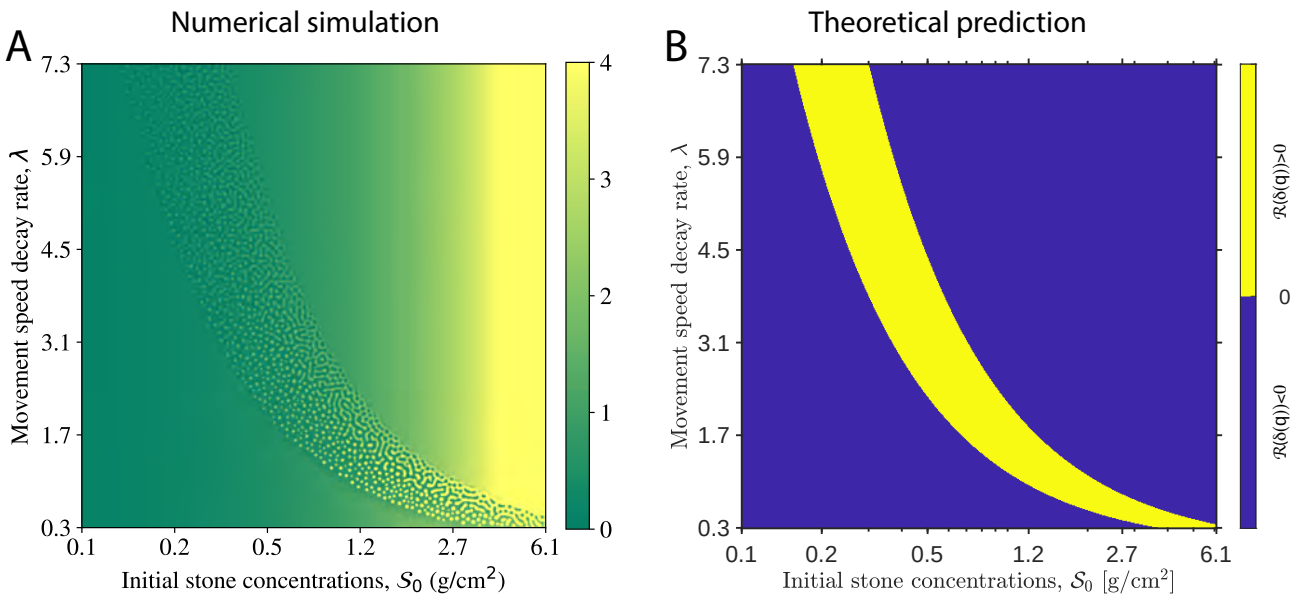

Fig. S16. Instability region of model 1 with linear stability analysis and numerical simulations. (A) Numerical simulation of phase separation Model 1. (B) The real part $\Re(\sigma(q))$ of the spatial eigenvalues in Eq. (S3.14) with $\gamma = 0.5$, ($\beta = 0.5v_0$, $v_0 = 2.02$, and $\kappa = 0.15$. Color bar: yellow region represents $\Re(\sigma(q)) > 0$, and blue $\Re(\sigma(q)) < 0$.

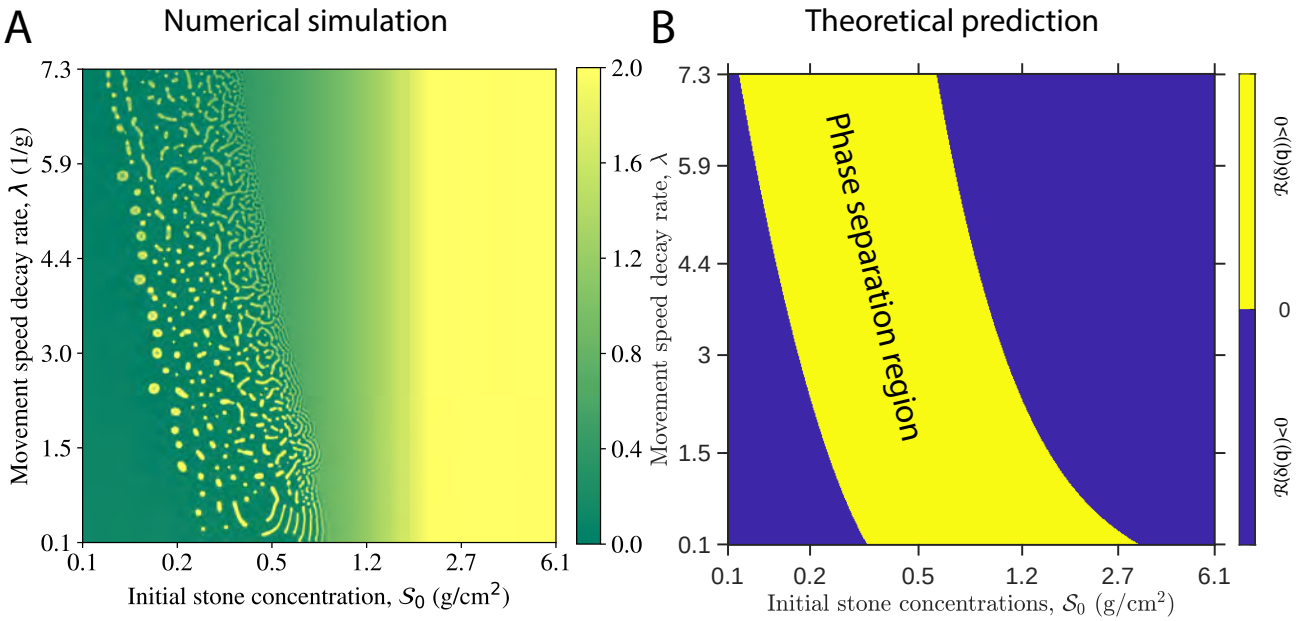

Fig. S17. Instability region of Model 2 with linear stability analysis and numerical simulations. (A) Numerical simulation of phase separation Model 2. (B) The real part $\Re(\sigma(q))$ of the spatial eigenvalues of Eq. (S3.17) with $\gamma = 0.5$, $\beta = 0.2$, $v_0 = 2.02$, and $\kappa = 0.05$. Color bar: yellow region represents more than 0, but blue less than 0.

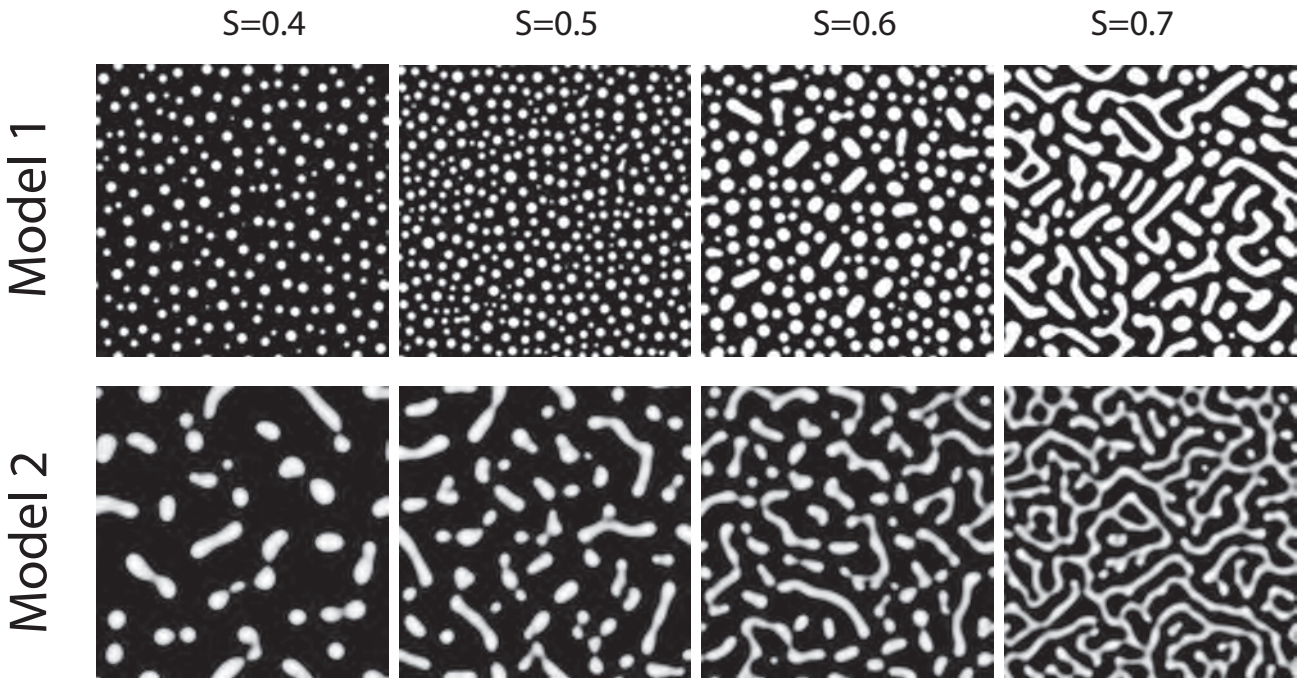

Fig. S18. Results of self-organized patterns with the quadratic function of stone speed, $v(\rho) = p_0 - p_1\rho + p_2\rho^2$. Snapshots show the spatial cluster at $t = 20000$ for Model 1 (*Top*) and Model 2 (*Bottom*). Parameter values are listed in Table S2, but for $p_1 = 3.8$. The codes are available from the GitHub (https://github.com/liuqx315/Phase-separation-patterned-ground).

S7. Supporting Information Movies

Movie S1. Movie of a stone pattern evolution produced by needle ice growth and decay at 30% stone cover on level ground (experiment 2, *SI Appendix*, Table S1) from top view. Overview of the pattern evolution with time, showing stones divergence, convergence, self-organization in pattern formation.

Movie S2. Movie of a stone pattern evolution produced by needle ice growth and decay at 40% stone cover on level ground (experiment 3, *SI Appendix*, Table S1) from top view. Overview of the pattern evolution with time, showing stones divergence, convergence, self-organization in pattern formation.

Movie S3. Movie of a stone pattern evolution produced by needle ice growth and decay at 60% stone cover on level ground (experiment 4, *SI Appendix*, Table S1) from top view. Overview of the pattern evolution with time, showing stones divergence, convergence, self-organization in pattern formation.

Movie S4. Movie of a stone pattern evolution during 15th freeze-thaw cycle at 40% stone cover on level ground (experiment 3, *SI Appendix*, Table S1) from side view. Overview of stone transport by needle ice growth and decay.

Movie S5. Movie of a pattern evolution arising from the phase separation model 1 of the Fig. 3A on the (S_0, λ)-space, where the other parameters were listed in *SI Appendix*, Table S3.

Movie S6. Movie of a pattern evolution arising from the phase separation model 2 of the Fig. 3B on the (S_0, λ)-space, where the other parameters were listed in *SI Appendix*, Table S3.

Movie S7. Movie of a stone pattern evolution produced by needle ice growth and decay at 80% stone cover on level ground (experiment 5, *SI Appendix*, Table S1) from top view. Overview of the pattern evolution with time, showing stones divergence, convergence, self-organization in pattern formation.

Movie S8. Movie of a stone pattern evolution produced by needle ice growth and decay at triple stone cover on level ground from top view. Overview of the pattern evolution with time, showing stones divergence, convergence, self-organization in pattern formation.

Movie S9. Movie of stone lift and transport by needle ice growth and decay at triple stone cover on level ground during first freeze-thaw cycle from side view.

References

1. AL Washburn, Classification of patterned ground and review of suggested origins. *Geol. Soc. Am. Bull.* **67**, 823 (1956).
2. P Bertran, L Klaric, A Lenoble, B Masson, L Vallin, The impact of periglacial processes on palaeolithic sites: The case of sorted patterned grounds. *Quat. Int.* **214**, 17–29 (2010).

3. T Uxa, P Mida, M Křížek, Effect of climate on morphology and development of sorted circles and polygons. *Permafr. Periglac. Process.* **28**, 663–674 (2017).
4. K Hall, Sorted stripes on sub-antarctic kerguelen island. *Earth Surf. Process. Landforms* **8**, 115–124 (1983).
5. SD Holness, The orientation of sorted stripes in the maritime Subantarctic, Marion Island. *Earth Surf. Process. Landforms: The J. Br. Geomorphol. Res. Group* **26**, 77–89 (2001).
6. SD Holness, Sorted circles in the maritime Subantarctic, Marion Island. *Earth Surf. Process. Landforms: The J. Br. Geomorphol. Res. Group* **28**, 337–347 (2003).
7. GY Jeong, Radiocarbon ages of sorted circles on King George Island, South Shetland Islands, West Antarctica. *Antarctic Sci.* **18**, 265–270 (2006).
8. CK Ballantyne, JA Matthews, The development of sorted circles on recently deglaciated terrain, Jotunheimen, Norway. *Arct. Alp. Res.* **14**, 341–354 (1982).
9. FC Ugolini, G Corti, G Certini, Pedogenesis in the sorted patterned ground of Devon plateau, Devon Island, Nunavut, Canada. *Geoderma* **136**, 87–106 (2006).
10. AL Washburn, Near-surface soil displacement in sorted circles, resolute area, Cornwallis Island, Canadian High Arctic. *Can. J. Earth Sci.* **26**, 941–955 (1989).
11. J Walters, Observations of sorted circle activity, central Alaska in *Proceedings of the 5th International Conference on Permafrost, Norway.* (1988).
12. P Sumner, Relict sorted patterned ground in Lesotho. *Permafr. Periglac. Process.* **15**, 89–93 (2004).
13. V Treml, M Krizek, Z Engel, Classification of patterned ground based on morphometry and site characteristics: A case study from the High Sudetes, Central Europe. *Permafr. Periglac. Process.* **21**, 67–77 (2010).
14. M Křížek, T Uxa, Morphology, sorting and microclimates of relict sorted polygons, krkonoše Mountains, Czech Republic. *Permafr. Periglac. Process.* **24**, 313–321 (2013).
15. S Winkler, et al., Schmidt-hammer exposure-age dating (shd) of sorted stripes on juvflye, jotunheimen (central south norway): Morphodynamic and palaeoclimatic implications. *Geomorphology* **353**, 107014 (2020).
16. J Obu, et al., Sorted patterned ground in a karst cave, ledenica pod hrušico, Slovenia. *Permafr. periglacial processes* **29**, 121–130 (2018).
17. B Francou, NL Méhauté, V Jomelli, Factors controlling spacing distances of sorted stripes in a low-latitude, alpine environment (Cordillera Real, 16 S, Bolivia). *Permafr. Periglac. Process.* **12**, 367–377 (2001).
18. T Caine, The origin of sorted stripes in the lake district, northern england. *Geografiska Annaler* **45**, 172–179 (1963).
19. J Warburton, N Caine, Sorted patterned ground in the english lake district. *Permafr. Periglac. Process.* **10**, 193–197 (1999).
20. N Matsuoka, M Abe, M Ijiri, Differential frost heave and sorted patterned ground: field measurements and a laboratory experiment. *Geomorphology* **52**, 73–85 (2003).
21. JB Benedict, *Field and laboratory studies of patterned ground in a Colorado alpine region.* (University of Colorado, Institute of Arctic and Alpine Research), (1992).
22. M Dabski, Small-scale sorted nets on glacial till, fláajökull (southeast iceland) and elisbreen (northwest spitsbergen). *Permafr. Periglac. Process.* **16**, 305–310 (2005).
23. AL Washburn, *Geocryology: A survey of periglacial processes and environments.* (Wiley), (1980).
24. A Li, N Matsuoka, F Niu, Frost sorting on slopes by needle ice: A laboratory simulation on the

effect of slope gradient. *Earth Surf. Process. Landforms* **43**, 685–694 (2018).
25. C Yamagishi, N Matsuoka, Laboratory frost sorting by needle ice: A pilot experiment on the effects of stone size and extent of surface stone cover. *Earth Surf. Process. Landforms* **40**, 502–511 (2015).
26. SP Anderson, The upfreezing process: Experiments with a single clast. *Geol. Soc. Am. Bull.* **100**, 609–621 (1988).
27. R Ray, W Krantz, T Caine, R Gunn, A model for sorted patterned-ground regularity. *J. Glaciol.* **29**, 317–337 (1983).
28. M Kessler, B Werner, Self-organization of sorted patterned ground. *Science* **299**, 380–383 (2003).
29. B Hallet, Stone circles: form and soil kinematics. *Philos. Transactions Royal Soc. A: Math. Phys. Eng. Sci.* **371**, 20120357 (2013).
30. J Schindelin, et al., Fiji: an open-source platform for biological-image analysis. *Nat. Methods* **9**, 676–682 (2012).
31. J van de Koppel, et al., Experimental evidence for spatial self-organization and its emergent effects in mussel bed ecosystems. *Science* **322**, 739–742 (2008).
32. JW Cahn, JE Hilliard, Free energy of a nonuniform system. i. interfacial free energy. *The J. chemical physics* **28**, 258–267 (1958).
33. A Higashi, AE Corte, Solifluction: A model experiment. *Science* **171**, 480–482 (1971).
34. ME Cates, D Marenduzzo, I Pagonabarraga, J Tailleur, Arrested phase separation in reproducing bacteria creates a generic route to pattern formation. *Proc. Natl. Acad. Sci. USA* **107**, 11715–11720 (2010).
35. MJ Schnitzer, Theory of continuum random walks and application to chemotaxis. *Phys. Rev. E* **48**, 2553 (1993).
36. J Tailleur, M Cates, Statistical mechanics of interacting run-and-tumble bacteria. *Phys. Rev. Lett.* **100**, 218103 (2008).
37. F Liu, N Goldenfeld, Dynamics of phase separation in block copolymer melts. *Phys. Rev. A* **39**, 4805–4810 (1989).
38. QX Liu, et al., Phase separation explains a new class of self-organized spatial patterns in ecological systems. *Proc. Natl. Acad. Sci. USA* **110**, 11905–11910 (2013).
39. M Rietkerk, J Van de Koppel, Regular pattern formation in real ecosystems. *Trends Ecol. & Evol.* **23**, 169–175 (2008).
40. AM Turing, The chemical basis of morphogenesis. *Philos. Transactions Royal Soc. Lond. Ser. B: Biol. Sci.* **237**, 37–72 (1952).
41. AA Hyman, CA Weber, F Jülicher, Liquid-liquid phase separation in biology. *Annu. Rev. Cell Dev. Biol.* **30**, 39–58 (2014).
42. S Boeynaems, et al., Protein phase separation: A new phase in cell biology. *Trends Cell Biol.* **28**, 420–435 (2018).
43. A Kääb, L Girod, I Berthling, Surface kinematics of periglacial sorted circles using structure-from-motion technology. *The Cryosphere* **8**, 1041–1056 (2014).
44. B Werner, B Hallet, Numerical simulation of self-organized stone stripes. *Nature* **361**, 142–145 (1993).
45. H Wickham, *ggplot2: Elegant graphics for data analysis*. (Springer-Verlag New York), (2016).
46. I Patil, Visualizations with statistical details: The 'ggstatsplot' approach. *Journal of Open Source Software* **6**, 3167 (2021).